TERAHERTZ MEASUREMENT OF THE

QUASIPARTICLE MASS RENORMALIZATION IN

LEAD AND CHROMIUM

by

Michael A. Gilmore

Bachelor of Science

Department of Physics, Western Washington University, 2001

Thesis submitted in partial fulfillment

of the requirements for the degree of

Master of Science

in the department

of

Physics

© Michael A. Gilmore 2004

SIMON FRASER UNIVERSITY

Fall, 2004

APPROVAL

Name:	Michael A. Gilmore
Degree:	Master of Science
Title of Thesis:	Terahertz Measurement of the Quasiparticle Mass Renormalization in Lead and Chromium
Examining Committee:	Dr. Howard Trottier, Professor, Department of Physics, SFU (Chair)

Dr. J. Steven Dodge, Assistant Professor,
Department of Physics, SFU

Dr. Jeff Sonier, Associate Professor,
Department of Physics, SFU

Dr. David Broun, Assistant Professor,
Department of Physics, SFU

Dr. Karen Kavanagh, Professor,
Department of Physics, SFU

Date Approved: November 30, 2004

SIMON FRASER UNIVERSITY

PARTIAL COPYRIGHT LICENCE

The author, whose copyright is declared on the title page of this work, has granted to Simon Fraser University the right to lend this thesis, project or extended essay to users of the Simon Fraser University Library, and to make partial or single copies only for such users or in response to a request from the library of any other university, or other educational institution, on its own behalf or for one of its users.

The author has further granted permission to Simon Fraser University to keep or make a digital copy for use in its circulating collection.

The author has further agreed that permission for multiple copying of this work for scholarly purposes may be granted by either the author or the Dean of Graduate Studies.

It is understood that copying or publication of this work for financial gain shall not be allowed without the author's written permission.

Permission for public performance, or limited permission for private scholarly use, of any multimedia materials forming part of this work, may have been granted by the author. This information may be found on the separately catalogued multimedia material and in the signed Partial Copyright Licence.

The original Partial Copyright Licence attesting to these terms, and signed by this author, may be found in the original bound copy of this work, retained in the Simon Fraser University Archive.

W. A. C. Bennett Library
Simon Fraser University
Burnaby, BC, Canada

Abstract

We study the optical conductivity of lead and chromium as a function of frequency and temperature using terahertz time-domain spectroscopy (THz-TDS). The optical conductivity is interpreted in terms of the extended Drude model (EDM), where the optical scattering rate and renormalized mass of the carriers take on frequency as well as temperature dependence. Within the EDM framework, the theory of electron-phonon scattering yields expressions for the optical scattering rate and mass enhancement, dependent upon the transport-weighted Eliashberg spectral function. This thesis presents THz-TDS measurements of thin films of Pb and Cr. We compare results for the optical scattering rate and quasiparticle mass renormalization to theory and find a strong agreement.

To my wife Sally.

Acknowledgments

I would like to give special thanks to the following people:

Steve Dodge- for your crucial insight and guidance which made this work possible.

Saeid Kamal- for your countless hours spent helping me make things work!

David Broun and Karen Kavanagh- for your insights and help with the lead film growth.

My wife Sally- for putting up with me.

Contents

List of Tables

List of Figures

Chapter 1

Introduction

Electrons in solids are correlated through a variety of mechanisms. Firstly, their charge yields correlation via the long-range Coulomb potential. Secondly, the Pauli exclusion principle results in an effective exchange force by requiring that no two electrons occupy the same quantum state. Electrons can also become correlated through the exchange of excitations in the system. These include phonons, magnons, and spin fluctuations.

As the band theory of solids demonstrates, the correlations may often be ignored without losing the essential description of the electron state. However, there are many instances where the correlations dominate and one must understand the mechanism to describe the state. Examples of such instances occur in highly-correlated electron systems such as conventional superconductors, high-temperature (unconventional) superconductors, and heavy-fermion materials.

It is well established that conventional superconductivity results from electron-phonon coupling. However, the correlation mechanisms present in high-temperature superconductors and heavy-fermion materials is a subject of great debate. While it is usually agreed that heavy-fermion materials are dominated by direct electron-electron interaction, the mechanism behind the high-temperature superconductors remains an open question. Recently, the literature has a large fraction of theories based on the electron-phonon interaction.

The understanding of complex systems always requires an existing knowledge of simpler systems. The study of electron correlations in conventional superconductors and other metals is incomplete. This thesis presents new results from Terahertz Time-Domain Spectroscopy (THz-TDS) on thin films of lead (Pb) and chromium (Cr). Pb is considered a

1

textbook example of a conventional superconductor ($T_c = 7.2\ K$). Though its superconducting properties have been well-studied, those of the normal state have not. In particular, those related to its strong electron-phonon coupling. Cr is a magnetic metal which does not superconduct. The electron coupling is thought to have both phonon and magnon contributions, which together exhibit a relatively weak coupling strength.

The outline of the thesis is as follows. The bare necessities of the theory which describes the coupled electron system are given in the following chapter. This includes the modelling of the electron-boson coupling in Pb and Cr, to which the THz-TDS results will be compared. Chapter 3 gives a brief introduction to the experimental aspects of THz-TDS and the specifications of our THz spectrometer. Here, the derivation of the relations between the optical fields in the experiment and the AC conductivity is given, along with insights into the consequences of using the standard approximation for the THz-TDS transfer coefficient. Chapter 4 then discusses the growth and characterization of the Pb samples. Finally, chapter 5 gives the experimental results and the conclusions of the comparison with theory.

Chapter 2

Electron Transport Theory

Ultimately, the theoretical treatment of electron transport properties of solids requires the solution of a state with 10^{23} particles. All particle dynamics must be described simultaneously because every particle is correlated via the long-range Coulomb interaction and the Pauli exclusion principle. This problem is impossible and one must resort to approximations in order to have an understanding of the fundamental physics. This chapter will review some aspects of electron transport in the presence of interactions and specifically treat the materials under consideration in this work.

2.1   The Quasiparticle Concept

When approaching a problem involving many quantum mechanical particles, one usually attempts to find a set of basis states in which the many-particle Hamiltonian is diagonal. The problem can then be formulated in terms of a single-particle Hamiltonian whose eigenstates are single-particle states. The many-particle state is constructed by the appropriately symmetrized direct product of single-particle states.

The nearly-free electron model is the simplest attempt at the description of electrons in a metal within a single-particle picture. In this model, the electrons make up a non-interacting gas which interacts with the periodic potential of the ions. The positions of the ions are fixed at their equilibrium positions (no phonons). The only electron-electron interaction results from the Pauli principle. If the ion potential was turned off, the electrons would fill a continuum of available energy eigenstates up to the Fermi energy. The presence

of the ion potential creates gaps in the available energy states. This is the origin of the band theory of solids. The highest occupied energy band is the conduction band. For a metal, this band is around half-full so that plenty of nearby states are available for electron transport.

In order to include interactions and still have a tractable problem, one is forced to redefine the particles in the system in such a way as they can be treated within a single-particle picture. The new particles are referred to as quasiparticles to distinguish them from the electrons. The electrons are said to be renormalized by the interaction, resulting in the quasiparticles. Physically, the quasiparticle is described as the electron plus the surrounding particle distortion due to the interaction. The quasiparticle and quasihole are the elementary excitations of the interacting system, analogous to the electron and hole of the noninteracting system.

An example of a similar type of redefinition of particles arises in the treatment of the two-body scattering problem. It is found that by taking the center-of-mass frame, the Hamiltonian takes the form of a single-particle Hamiltonian. This Hamiltonian describes a quasiparticle with a mass equal to the reduced mass of the particles and a position equal to the center-of-mass of the particles.

2.2 Quasiparticle Renormalization

In order to further understand the manner in which the electrons are renormalized by interactions, we will appeal to concepts of Landau's Fermi-Liquid theory (see Pines and Nozières [32]). The premise is that the eigenstates of the interacting system may be generated from the eigenstates of the noninteracting system by adiabatically turning on the interactions. The discussion assumes low temperatures where the excited electrons are close to the Fermi surface.

We begin with the set of states $\{p, \varepsilon_p\}$ of the noninteracting system, where p and ε_p are the momentum and energy of the electron. When the interactions are slowly turned on, the eigenstates smoothly evolve into the set $\{p, E_p\}$, where E_p is the quasiparticle energy. The relation between these quantities is given by

$$E_p = \frac{\varepsilon_p}{1 + \lambda_0} \tag{2.1}$$

The mass enhancement factor λ_0 characterizes the strength of the interaction. For $\lambda_0 = 0$,

the energies are equal, signifying the absence of renormalization. As the interactions are turned on, λ_0 becomes larger and the quasiparticle energy decreases.

The velocity of the quasiparticle excitation is defined as

$$v^* = \nabla_p E(p) = \frac{1}{1 + \lambda_0} \nabla_p \varepsilon(p) \tag{2.2}$$

which shows that it is also renormalized by the interaction. The quasiparticle mass m^* is naturally defined by the relation $v^* = p/m^*$. The band mass m_b, which accounts for the effects of the periodic potential of the ions of the lattice on the free-electron dispersion, is given by the same relation as m^*, but with a velocity that has not been renormalized. Thus we have

$$\frac{m^*}{m_b} = 1 + \lambda_0 \tag{2.3}$$

which shows where λ_0 gets its name. We stress that the momentum p is not renormalized since it is the quantum number that labels both the corresponding eigenstates of the noninteracting and interacting systems.

The velocity renormalization also results in the renormalization of the lifetime of the quasiparticle state. For a fixed mean free path, the lifetime must be enhanced by the same factor that the velocity is reduced. Denoting the lifetime of the state $\{p, \varepsilon_p\}$ by τ_p, we have

$$\frac{\tau_p^*}{\tau_p} = 1 + \lambda_0 \tag{2.4}$$

One refers to $1/\tau_p$ and $1/\tau_p^*$ as the unrenormalized and renormalized quasiparticle scattering rates, respectively. The notion of the mean free path remaining the same while the velocity and lifetime are renormalized is clearly only valid for impurity scattering. However, Prange and Kadanoff [33] show that Equation 2.4 is required for *any* scattering process. The dynamical conductivity discussed in the following section provides direct access to an optical version of τ_p^*.

Many-particle systems where the quasiparticle picture holds together are termed Fermi liquids. That is, in appropriate limits (small $\omega\tau$) they can be considered to be a system of weakly interacting fermions. Systems where this picture fails are non-Fermi liquids. Both lead and chromium are textbook examples of Fermi liquids.

2.3 The Dynamical Conductivity

The optical conductivity contains a wealth of information regarding carrier dynamics. In order to extract the information, one must rely on models of electron transport.

2.3.1 Drude Model

The Drude model is perhaps the simplest model of electrical conduction in a metal. Although its original derivation was from an overly-naive classical picture of electrons scattering from static ions, it can be more rigorously derived from the Boltzmann equation within the relaxation time approximation [40].

The Boltzmann equation is a semiclassical description of the rate of change in the electron momentum distribution $f_k(r)$ at a point r in space. It defines several causes for the rate of change; external electric and magnetic fields, temperature gradients, diffusion, and scattering. In a steady state, these rates sum to zero. While all the terms are (classically) easy to describe, the scattering term is difficult and requires a microscopic (quantum) description. The simple Drude theory arises from the Boltzmann equation when we take

$$-\left[\frac{\partial f_k}{\partial t}\right]_{scatt} = \frac{1}{\tau_0}(f_k - f_k^0) \qquad (2.5)$$

where $1/\tau_0$ is an optical scattering rate and f_k^0 is the equilibrium distribution, given by the Fermi function. This is referred to as the relaxation time approximation. The distinction between optical scattering rates and quasiparticle scattering rates will be addressed later.

Including the temperature dependence of τ_0, the expression for the dynamical conductivity $\sigma(\omega, T)$ in the Drude model is given by

$$\sigma(\omega, T) = \frac{\omega_p^2 \varepsilon_0}{1/\tau_0(T) - i\omega} \qquad (2.6)$$

where ω_p is the plasma frequency and ε_0 is the permittivity of free space. The square of the plasma frequency is proportional to the integral of the carrier velocity over the Fermi surface. For a spherical Fermi surface we have

$$\omega_p^2 \varepsilon_0 = \frac{ne^2}{m} \qquad (2.7)$$

where n is the carrier density and m is the carrier mass. For real materials, the band mass m_b is substituted.

The Drude conductivity may also be written as $\sigma(\omega) = \sigma_1(\omega) + i\sigma_2(\omega)$, where

$$\sigma_1(\omega) = \omega_p^2 \varepsilon_0 \frac{\tau_0}{1 + (\omega\tau_0)^2} \quad \text{and} \quad \sigma_2(\omega) = \omega_p^2 \varepsilon_0 \frac{\tau_0^2 \omega}{1 + (\omega\tau_0)^2} \tag{2.8}$$

Thus, the real part of the conductivity is described as a Lorentzian peak centered at zero frequency whose width is determined by $1/\tau_0$ and oscillator strength determined by ω_p. At low frequencies, the imaginary part is linear in frequency, with a slope of $1/\tau_0$ and a zero intercept.

The DC conductivity is the zero frequency limit of Equation 2.6 given by

$$\sigma_0(T) = \frac{ne^2\tau_0(T)}{m_b} \tag{2.9}$$

for a spherical Fermi surface. The resistivity is given by $\rho(T) = 1/\sigma_0(T)$. It is apparent from Equations 2.4 and 2.3 that if the lifetime and mass are both renormalized by interactions, the factors of $1 + \lambda_0$ will cancel. Thus, the DC conductivity shows no effects of renormalization. This is a specific example of a more general result derived by Prange and Kadanoff [33].

2.3.2 The Memory Function Formalism

Of course, the relaxation time approximation is not always valid. The presence of interactions results in more complicated scattering events which give structure to the relaxation. In an attempt to include these scattering events, the Drude model of Equation 2.6 can be generalized by letting the damping term be complex and frequency dependent. This term is usually defined as the memory function $M(\omega, T)$. In order to see how such a term can arise, we go back to the Boltzmann equation. Instead of the relaxation time approximation of Equation 2.5, we let

$$-\left[\frac{\partial f_{\mathbf{k}}}{\partial t}\right]_{\text{scatt}} = \int_{-\infty}^{\infty} dt' \tilde{M}(t - t', T)(f_{\mathbf{k}}(t') - f_{\mathbf{k}}^0) \tag{2.10}$$

where the tilde denotes the Fourier transform

$$M(\omega, T) = \int_{-\infty}^{\infty} \tilde{M}(x, T) \exp(i\omega x) dx \tag{2.11}$$

Here, $\tilde{M}(x, T)$ is real and $\tilde{M}(x < 0, T) = 0$. In the absence of the field, we no longer have the simple exponential decay of the distribution function to its equilibrium as we did in the relaxation time approximation. The two expressions of the scattering term are equivalent when $\tilde{M}(t, T) = \frac{1}{\tau(T)}\delta(t)$. The conductivity from the Boltzmann equation using Equation 2.10 is

$$\sigma(\omega, T) = \frac{\omega_p^2 \varepsilon_0}{M(\omega, T) - i\omega} \tag{2.12}$$

Of course, this approach is far too simplified. However, it is noted by J. W. Allen *et al* [3] that microscopic quantum transport calculations often lead to Boltzmann-type equations. Here the Boltzmann equation is a simple means to obtain a generalized Drude form which is causal. Mori [27] has derived a similar form for $\sigma(\omega)$ using a general analysis of time-correlation functions.

The form of Equation 2.12 has also been obtained by a weak-coupling approximation of an explicit many-body treatment of electron scattering from a bosonic excitation in metals [11][4][23]. This treatment gives

$$M(\omega, T) = 1/\tau_{imp} - 2i \int_0^\infty d\Omega B(\Omega) K\left(\frac{\omega}{2\pi T}, \frac{\Omega}{2\pi T}\right) \tag{2.13}$$

where

$$K(x, y) = \frac{i}{y} + \left\{\frac{y - x}{x}[\Psi(1 - ix + iy) - \Psi(1 + iy)]\right\}$$
$$+ \left\{\frac{y + x}{x}[\Psi(1 - ix - iy) - \Psi(1 - iy)]\right\} \tag{2.14}$$

The function $B(\omega)$ describes the coupling of the electrons to the bosonic excitation, Ψ is the digamma function, and $1/\tau_{imp}$ is the impurity scattering rate. In the case of electron-phonon coupling, $B(\omega)$ is the transport-weighted Eliashberg spectral function $\alpha_{tr}^2 F(\omega)$. In the case of spin fluctuations, $B(\omega)$ is proportional to the imaginary part of the magnetic susceptibility. Equation 2.13 will be used to model the materials under consideration in this thesis. Kaufmann *et al* [23] give a comparison between the conductivity obtained using Equations 2.12 and 2.13 and a more general form of the conductivity used to derive them. The differences are small and the merit of the memory function is supported.

2.3.3 The Extended Drude Model

In the extended Drude model (EDM), the memory function is assumed to be

$$M(\omega, T) = \tau^{-1}(\omega, T) - i\omega\lambda(\omega, T) \tag{2.15}$$

where $\tau^{-1}(\omega, T)$ is the optical scattering rate and $\lambda(\omega, T)$ is the (dynamic) optical mass enhancement. The conductivity takes the form

$$\sigma(\omega, T) = \frac{\omega_p^2 \varepsilon_0}{\tau(\omega, T)^{-1} - i\omega\{1 + \lambda(\omega, T)\}} \tag{2.16}$$

If $\lambda(0, T) \ll 1$, the EDM reduces to Equation 2.6 for low frequencies.

The choice of the terms τ^{-1} and λ used for the real and imaginary parts of the memory function stems from its close analogy to the electron self-energy $\Sigma(\omega, T)$ used in many-body theory. The self-energy modifies the single-electron energy to include the effects of interactions. For a Fermi liquid we have [22]

$$i\Sigma(\omega, p, T = 0) \approx \frac{1}{2\tau_p} - i\omega\lambda_0 \tag{2.17}$$

The complete relation between the memory function given by Equation 2.13 and the self-energy has not been derived. In particular, the optical scattering rate $\tau^{-1}(\omega, T)$ and the unrenormalized quasiparticle scattering rate $1/\tau_p$ are not simply related. The essential difference is that τ^{-1} comes from a Fermi surface average with a $1 - \cos\theta$ weighting factor along the direction of the optical field [22]. That is, the scattering probability is greater for larger angle scattering events. This is often referred to as transport-weighting.

Allen [5] discusses the use of a transport-weighted self-energy $\Sigma_{tr}(\omega, T)$, which has a simpler relation to the memory function. Sher [36] has done numerical calculations for Pb which indicate that the difference between $\Sigma_{tr}(\omega, T)$ and $\Sigma(\omega, T)$ is small. In the limit of low frequencies and temperatures, Allen derives the following

$$-iM(\omega, T) \approx \Re\Sigma_{tr}(\omega, T) + 2i\Im\Sigma_{tr}(\omega, T) \tag{2.18}$$

The analytic properties of M and Σ_{tr} are very similar, with the most obvious difference being the factor of two in the imaginary part. In terms of the EDM parameters, we can

write

$$\lambda(\omega, T) \approx -\frac{d\Re\Sigma_{tr}(\omega, T)}{d\Omega} \qquad (2.19)$$

$$1/\tau(\omega, T) \approx -2\Im\Sigma_{tr}(\omega, T) \qquad (2.20)$$

Comparing to Equation 2.17, $\lambda(\omega, T)$ and $\tau(\omega, T)$ are transport versions of λ_0 and τ_p in the low frequency and temperature limit. The derivative was used to express $\lambda(\omega, T)$ in reference to the usual definition of λ_0 [22]. We see that $1/\tau(\omega, T)$ plays the role of an *unrenormalized* scattering rate. It is stressed that Equation 2.18 only holds for low frequencies and temperatures. Some discussion of the relation between M and Σ_{tr} at higher frequencies is given by Shulga *et al* [37].

It is instructive to examine Equation 2.13 in the limit of low frequency and temperature. For the imaginary part, we find that

$$\lim_{\omega \to 0, T \to 0} \Im\left[\frac{i}{\omega}\right] K\left(\frac{\omega}{2\pi T}, \frac{\Omega}{2\pi T}\right) = \frac{1}{\Omega} \qquad (2.21)$$

so that

$$\lambda(0,0) = 2\int_0^\infty d\Omega \frac{\alpha_{tr}^2 F(\Omega)}{\Omega} \qquad (2.22)$$

This is analogous to the well-known equation for λ_0 in terms of the isotropically-weighted Eliashberg function [22]. The corresponding limit of the real part simply yields $1/\tau_{imp}$.

The simple Drude form of Equation 2.6 is also sometimes generalized by defining a renormalized optical scattering time $\tau^*(\omega, T) = \tau(\omega, T)(1 + \lambda(\omega, T))$. In order to maintain a causal Drude conductivity, a renormalized plasma frequency $\omega_p^2(\omega, T) = \omega_p^2/(1 + \lambda(\omega, T))$ must also be defined. The disadvantage of this interpretation is that the scattering rate is not causal and its physical interpretation is more difficult since it includes both velocity renormalization and lifetime effects [34]. In the EDM, the mass enhancement factor describes the velocity renormalization while the scattering rate describes only lifetime effects.

A useful relation between the real and imaginary parts of the memory function is given by requiring that the conductivity is causal. The Kramers-Kronig relations [40] then give $\lambda(\omega, T)$ in terms of $\tau(\omega, T)$ as

$$\lambda(\omega, T) = \frac{2}{\pi}\wp\int_0^\infty \frac{\tau^{-1}(\Omega, T)}{\Omega^2 - \omega^2} d\Omega \qquad (2.23)$$

where $\wp$ denotes the Cauchy Principal Value of the integral. It requires a knowledge of $\tau(\omega)$ at all frequencies in order to calculate $\lambda(\omega)$. It is important to see that the impurity scattering does not effect λ since

$$\wp \int_0^\infty \frac{dx}{x^2-c^2} = \frac{1}{2c} \lim_{\delta\to 0} \left\{ \ln\left(\frac{x-c}{x+c}\right) \Big|_0^{c-\delta} + \ln\left(\frac{x-c}{x+c}\right) \Big|_{c+\delta}^\infty \right\} = 0 \qquad (2.24)$$

Thus, the renormalization parameter is independent of the residual resistivity. This fact gives some reassurance that films of reasonable quality should display the same mass renormalization as a perfect film.

2.4 Modelling Simple Metals

This section provides a theoretical description of the optical conductivity for Pb and Nb. Though only the Pb results will be compared with experiment, the results for Nb serve as a further illustration and for use in future work. The analysis makes use of Equations 2.12 and 2.13 and closely follows the work by Puchkov *et al* [34].

2.4.1 The Eliashberg Function

In order to calculate the memory function using Equation 2.13, one must first decide on the form of the bosonic coupling function $B(\omega)$. In simple metals, the electron-impurity and electron-phonon scattering dominates, so that $B(\omega)$ should be the transport-weighted Eliashberg spectral function $\alpha_{tr}^2 F(\omega)$ [4].

A few versions of the Eliashberg spectral function can be found in the literature. The isotropically-weighted Eliashberg function $\alpha^2 F(\omega, k)$ describes the scattering from a point (k, E_k) to all other final states $(k', E_{k'})$ such that $E_{k'} = E_k \pm \hbar\omega$. Assuming the scattering is isotropic, the dependence on k is dropped. The only factors which contribute are the density of states at the Fermi energy and the probability of an electron scattering by the emission of a phonon. Figure 2.1 (a) shows tunnelling data for $\alpha^2 F(\omega, k)$ as a function of frequency in THz for pure Pb (solid) and Nb (dashed) [26]. The peaks arise from the acoustic transverse and longitudinal phonons. For Pb, the transverse is located at 4.4 meV=1.06 THz and the longitudinal at 8.4 meV=2.03 THz. The phonon density of states $F(\omega)$ is very similar to $\alpha^2 F$ with a slightly larger amplitude [26].
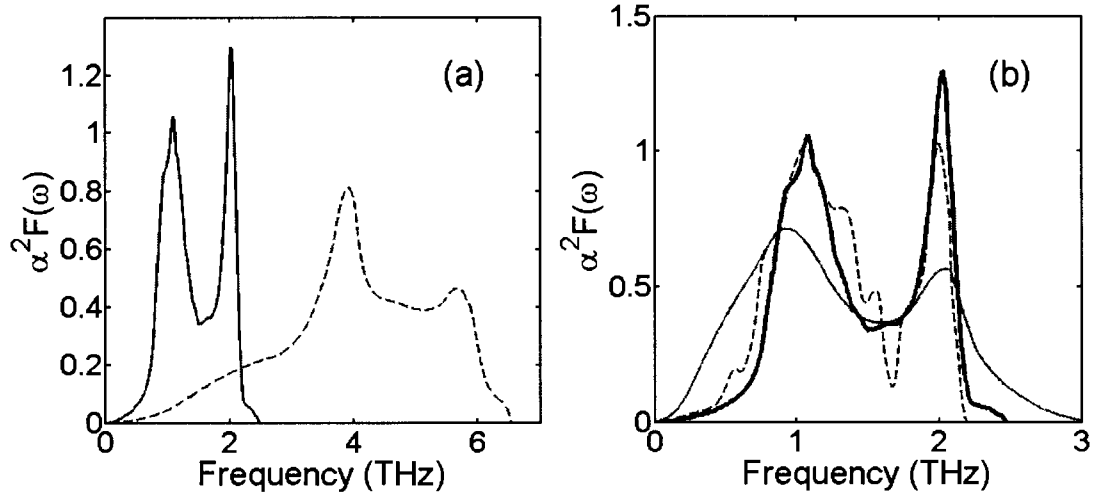
Figure 2.1: Experimental measurements of the Eliashberg spectral function. Plot (a) shows results of tunnelling measurements performed on crystalline samples of Pb (solid) and Nb (dashed) [26]. Plot (b) shows a comparison between tunnelling data for single-crystalline (thick solid) [26] and disordered (thin solid) [24] Pb samples and infrared reflectivity data for single-crystalline Pb (dashed) [20].

The appropriate Eliashberg function for transport properties is the transport-weighted Eliashberg function $\alpha_{tr}^2 F(\omega)$. The weighting is identical to that of the optical scattering rate discussed earlier. Allen [4] points out that for low frequencies, $\alpha^2 F \propto \omega^2$ while $\alpha_{tr}^2 F \propto \omega^4$. At higher frequencies, the spectra are similar, with the transverse peak more heavily weighted than the longitudinal. Farnworth and Timusk [20] calculate $\alpha_{tr}^2 F(\omega)$ from the inversion of infrared reflectivity data and obtain a spectrum which agrees with Allen qualitatively, with the magnitude of the longitudinal peak being reduced by 20% of the longitudinal peak in $\alpha^2 F$ from tunnelling data. The dashed and thick solid curves of Figure 2.1 (b) show the comparison of the data from Farnworth and Timusk and the tunnelling data, respectively.

The effect of disorder on the Eliashberg function has been considered by Leslie *et al* [24]. The thin solid curve in Figure 2.1 (b) shows the $\alpha^2 F(\omega)$ extracted from tunnelling data for disordered Pb. The Pb films of the tunnel junction were grown by thermal evaporation onto a substrate held at 1.4 K. When annealed, the measured Eliashberg functions took the form shown by the thick solid line in Figure 2.1.

Table 2.1 shows a characterization of the Eliashberg functions for Pb and Nb. The

material	$< \omega > meV$	λ_0
Pb (crystalline)	5.16	1.55
Pb (disordered)	4.05	2.10
Pb (infrared)	4.70	1.76
Nb (crystalline)	14.4	1.02

Table 2.1: Values of $< \omega >$ and λ_0 for Pb and Nb.

quantity $< \omega >$ is a measure of the characteristic coupling frequency which is often seen in the literature. It is part of a larger group of frequencies defined by

$$< \omega^n > = \frac{\int_0^\infty \omega^{n-1}\alpha^2 F(\omega)d\omega}{\int_0^\infty \omega^{-1}\alpha^2 F(\omega)d\omega} \tag{2.25}$$

with n a positive integer. The parameters were calculated directly from the Eliashberg functions shown in Figure 2.1 using Equations 2.25 and 2.22.

2.4.2 Calculations

In order to illustrate the qualitative behavior of the memory function, we first calculate it using Equation 2.13 with a square bosonic spectral function; $B(\omega) = A_0$ in the frequency range $\{1/2..3/2\}\omega_0$ where ω_0 is a center coupling frequency, and zero outside this frequency range. By defining the value of λ_0, the value of A_0 can be set using Equation 2.22. Using Equation 2.25, we have $< \omega > = \omega_0/\ln(3)$.

Assuming $\lambda_0=1.55$ and no impurity scattering, the results of the calculations are shown in Figure 2.2. All frequencies, temperatures, and scattering rates are given in units of ω_0. Plot (a) shows the Eliashberg function vs. frequency. Plot (b) shows the scattering rate vs. frequency for temperatures of 0, 0.125, 0.25, 0.5, and 1.0, shown by the thick solid, dashed, thin solid, dashed, and thin solid, respectively. Plot (c) shows $\lambda(\omega, T)$ vs. frequency for the same sample of temperatures. Above $T = 1.0$, the value of λ is small and the frequency dependence of both λ and $1/\tau$ is weak. These plots emulate those given by Puchkov et al [34]. Figure 2.2 (d) shows $\lambda(\omega, T)$ vs. temperature for frequencies 0, 0.3, 0.6, 0.9, and 1.2, shown by the thick solid, dashed, thin solid, dashed, and thin solid lines, respectively. Since these curves are very similar, only the 0 and 1.2 frequency curves are labelled. Frequencies

above 1.2 are not shown since we will find that the THz-TDS experiment probes at or below the characteristic frequency. The $\lambda(\omega, T)$ plots show that λ_0 is approached in the low frequency and temperature limit.

We now apply Equation 2.13 to Pb. The Eliashberg function is taken to be the single-crystalline tunnelling version shown as the solid curve in Figure 2.1 (a). The solid curves of Figure 2.3 show the optical scattering rate in plot (a) and dynamic mass enhancement in plot (b) versus frequency for the temperatures 8 K, 12 K, 20 K, 30 K, and 80 K. In units of $<\omega>=5.16$ from Table 2.1, this temperature range is 0.13-1.3, similar to the range in Figure 2.2. We will later see that the THz-TDS experiment only probes the conductivity below 1 THz, where the frequency dependence of $1/\tau$ and λ is weak. The noise contributions in the experiment will make the detection of this frequency dependence impossible.

The open circles in Figure 2.3 show the calculations with a square Eliashberg function which has been scaled so that $<\omega>$ and λ_0 match the values for the crystalline Pb in Table 2.1. We see that the modification due to the form of the spectral function is fairly small in the mass enhancement and negligible in the scattering rate. This is because the essential parameters of the spectral functions are the same. Following the discussion earlier, we may conclude that the approximation of the transport-weighted spectral function by the isotropically-weighted spectral function should result in a negligible difference in the values of $1/\tau(\omega, T)$ and $\lambda(\omega, T)$.

If we also perform the calculations for Nb using the crystalline Eliashberg function, we find that the forms of $1/\tau(\omega, T)$ and $\lambda(\omega, T)$ are very similar, differing only by the effective scaling by λ_0 and $<\omega>$. Figure 2.4 shows the temperature dependence of the dynamic mass enhancement for Pb and Nb. Plot (b) shows a scaled version of plot (a), with temperature in units of $<\omega>$ and $\lambda(\omega, T)$ in units of λ_0. The frequencies plotted are 0.2, 0.4, 0.6, 0.8, and 1.0 THz in plot (a) and 0.6 THz in plot (b).

Plot (a) again shows that the frequency dependence of λ is very weak within the THz-TDS frequency range of 0-1 THz. The difference between the frequency curves is only apparent at very low temperatures, where the theory is no longer valid due to the superconducting transition. The difference between the curves of plot (b) is also only apparent at very low temperatures. This supports the use of any approximate form for the Eliashberg function, as long as the parameters λ_0 and $<\omega>$ are accurate. In addition, we find that the effect of using the spectral function for disordered Pb is only apparent below 10 K, where
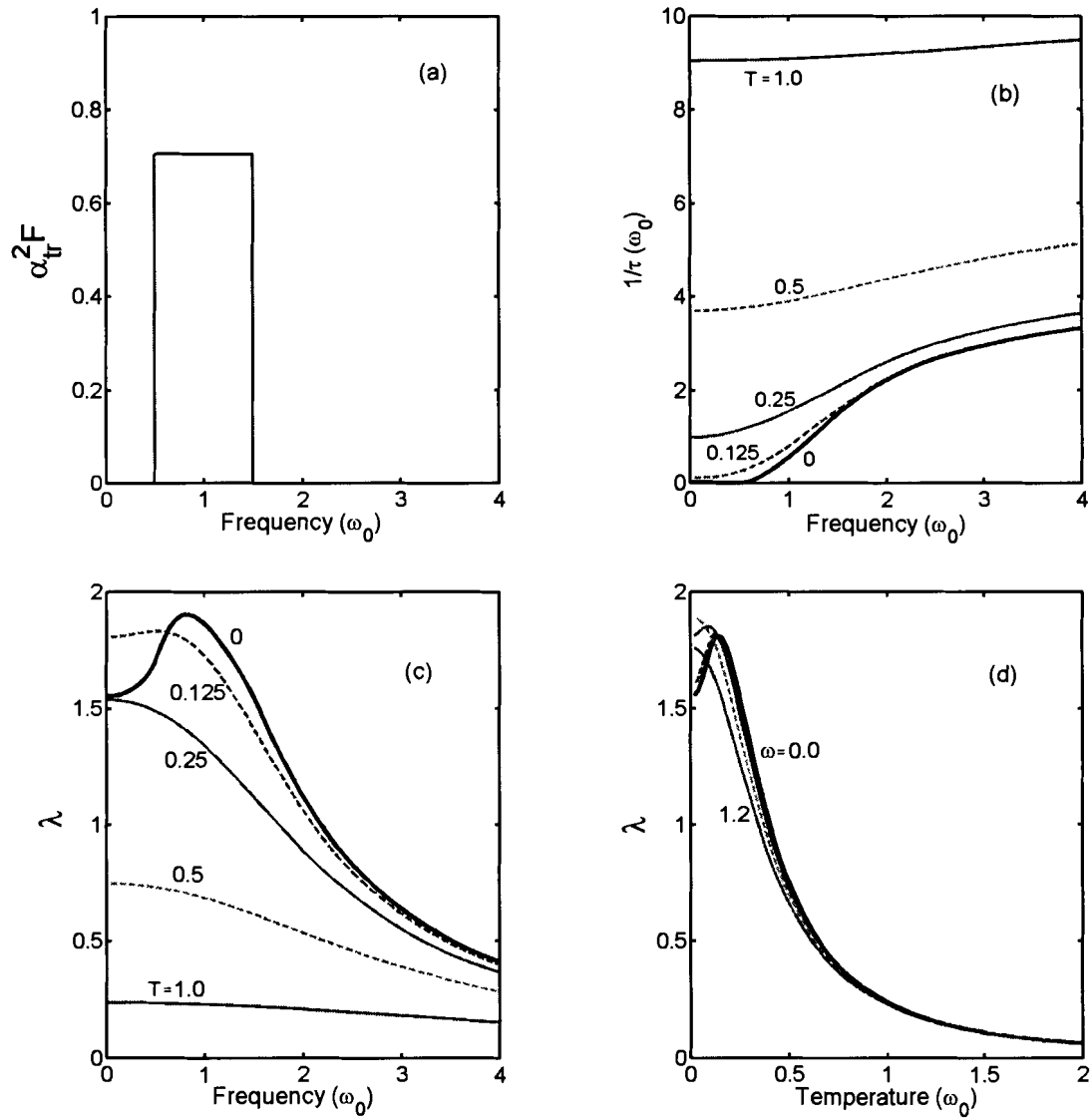
Figure 2.2: Plot (a) shows the square Eliashberg function used. Plots (b) and (c) show the optical scattering rate and mass enhancement as a function of frequency for the temperatures labelled in the plots. Plot (d) shows the optical mass enhancement as a function of temperature for frequencies within $0\text{-}1.2\omega_0$.
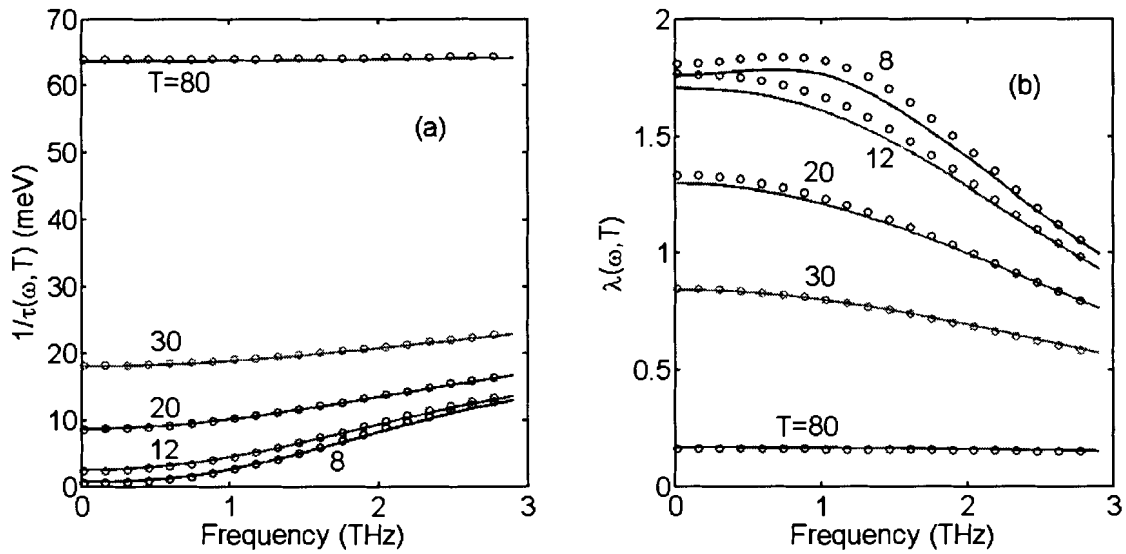
Figure 2.3: The optical scattering rate and dynamic mass enhancement for Pb (solid curve) and a square Eliashberg function (open circles).
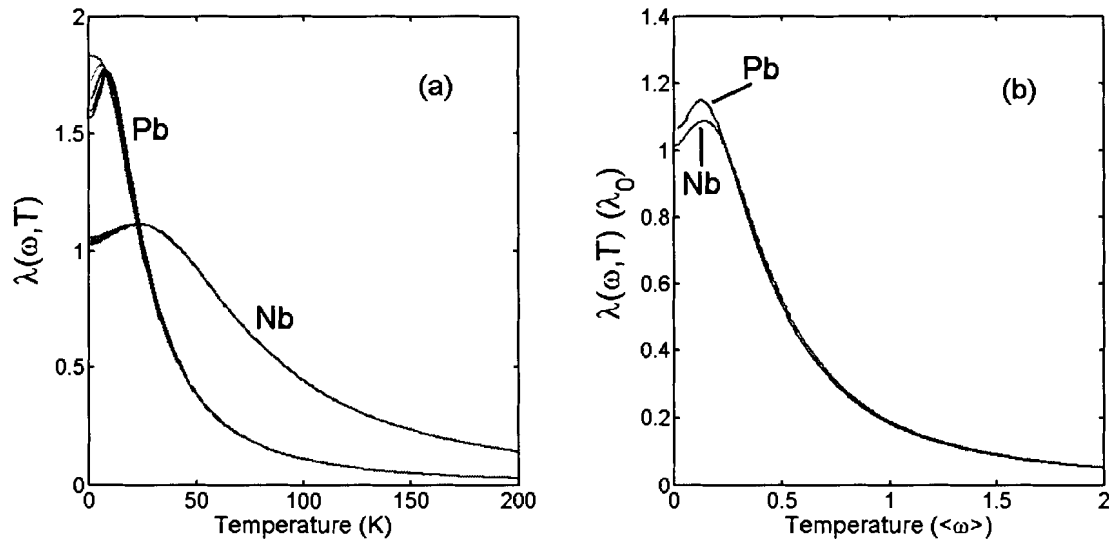
Figure 2.4: Plot (a) shows the dynamic mass enhancement as a function of temperature (K) for Pb and Nb for frequencies in the range 0.2-1.0 THz. Plot (b) shows the same plot for $\omega=0.6$ THz with the axes in units of λ_0 and $< \omega >$.
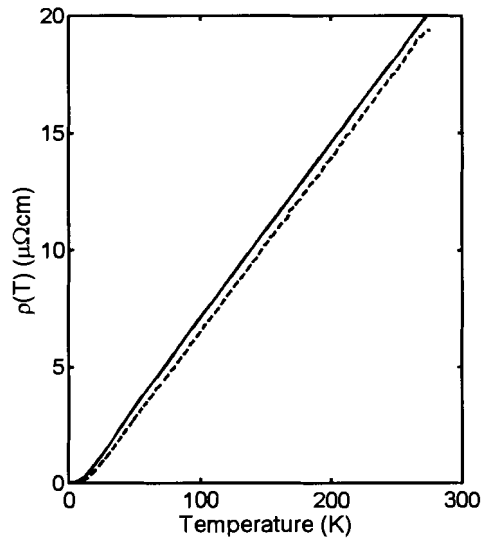
Figure 2.5: DC resistivity as a function of temperature for Pb. The solid line shows the theory while the dashed shows experimental data on bulk Pb [1].

the disordered version becomes larger. This is due to λ_0 increasing while $< \omega >$ decreases. The combined effect is negligible at temperatures we will observe.

The DC resistivity can be calculated from the scattering rate if a plasma frequency is assumed. Figure 2.5 shows a plot of the theory (solid) assuming $\omega_p = 9.2$ eV and an experimental measurement on bulk Pb (dashed) [1]. The plasma frequency was chosen so that the slopes of the resistivities match at high temperatures. The values of the plasma frequency listed in the literature vary from 7.4 eV [15] to 9.6 eV [9]. The former is an infrared reflectivity measurement and the latter is from theory. These values tend to be inaccurate and therefore we shall assume the value of 9.2 eV from this point forward.

2.5 Modelling Chromium

This section develops a model of the optical conductivity of Cr, which will be used as a comparison to the THz-TDS measurements presented in chapter 5. The behavior of Cr is more difficult to model than Pb or Nb primarily because of its magnetic properties. The
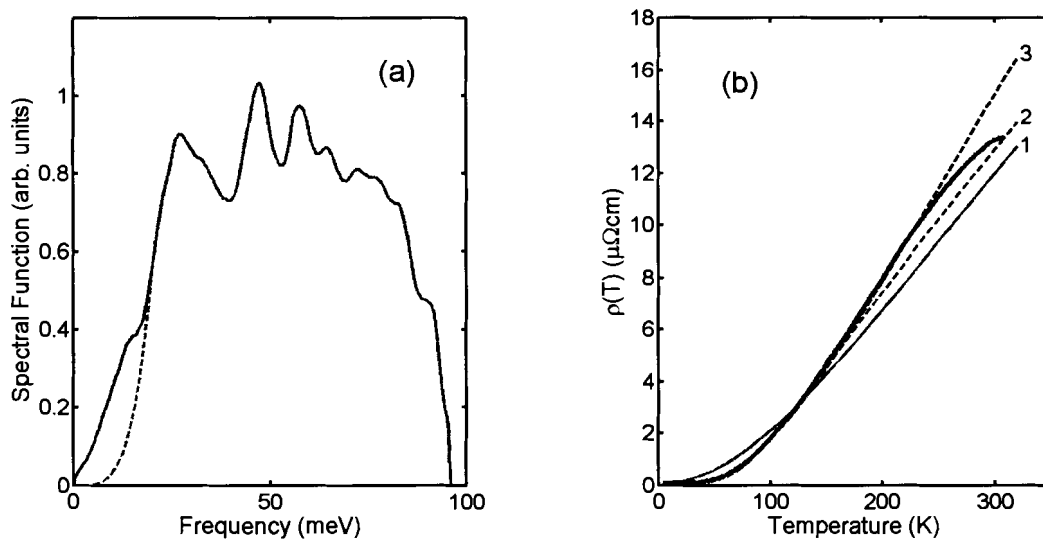
Figure 2.6: Plot (a) shows two of the bosonic spectral functions proposed for Cr [13]. Plot (b) shows the DC resistivity calculated using Gerasimenko's spectral function (1) and two alternative spectral functions (2,3) and compares them to experiment (thick solid line) [6].

scattering of electrons from magnons as well as phonons is thought to contribute to the spectral function [13]. Further complicating the situation is the paramagnetic to antiferromagnetic transition at 310 K [2], creating a kink in the resistivity as a function of temperature. Thus, our goal will not be a complete description of Cr, but one that will allow a qualitative comparison with the renormalization shown by the THz-TDS data.

The model memory function in Equation 2.13 is meant for any electron-boson scattering. Thus, one might attempt to model Cr with the use of a spectral function which includes both magnon and phonon contributions. Gerasimenko *et al* [13] have obtained the shape of this spectral function by analysis of electron tunnelling data. However, the magnitude cannot be determined because the theory for the interpretation of the electron-tunnelling only describes a proportionality. The spectral function is shown as the solid line in Figure 2.6 (a). Gerasimenko comments that, from neutron measurements, the phonon frequency cuts off at around 40 meV, so that the weight above that frequency must be due to magnons.

Unlike the case of Pb, both the plasma frequency *and* the magnitude of the coupling are unknown. The literature values of λ_0 range from 0.13 [18] to 0.5 [29] and values for the

plasma frequency are too inaccurate. We can however relate these parameters to each other through the DC resistivity. The high-temperature resistivity is linear with the dependence

$$\rho(T) \propto \frac{\lambda_0}{\omega_p^2} T \qquad (2.26)$$

Thus, the ratio λ_0/ω_p^2 can be estimated by fitting the theory to a bulk Cr experimental resistivity. We shall quote values for this ratio in $1/eV^2$.

The result of Equation 2.13 for the DC resistivity using Gerasimenko's spectral function is shown as the thin solid line labelled (1) in Figure 2.6 (b). This is to be compared with the experimental curve [6] shown as the thick solid line. The ratio has been set to 0.012 and the value of $< \omega > = 36$ meV. The curves can only be expected to agree well below the antiferromagnetic transition at 310 K. Still, the discrepancy between the curves is substantial and cannot be corrected by scaling.

It is useful to consider the properties of a spectral function which would yield a better agreement with the experimental resistivity. First, we consider a delta function. This is instructive since it simplifies the spectrum to the essential parameters, $< \omega >$ and λ_0. The values of λ_0/ω_p^2 and $< \omega >$ can be adjusted to fit the resistivity. The result is shown as the dashed curve labelled (2) in Figure 2.6 (b). The theory and experiment are essentially indistinguishable up to 150 K. The parameters for the delta function have been determined to be $\lambda_0/\omega_p^2 = 0.0123 \pm 0.0006$ $1/meV^2$ and $< \omega > = 32 \pm 1$ meV. Within the error ranges given, the difference between the calculated and experimental resistivities remains less than 0.1 $\mu\Omega$ cm for temperatures 0 to 160 K.

It is also useful to consider a transport-modified version of Gerasimenko's spectral function. As mentioned earlier, Allen describes the typical behavior of a transport-weighted spectral function at low frequencies by ω^4. Gerasimenko's spectral function has almost a linear dependence up to its transverse phonon peak at 27 meV, which significantly weights that region. This manifests itself by prematurely increasing the resistivity at low temperatures. We modify Gerasimenko's function by substituting the ω^4 dependence as an approximate transport-weighting procedure.

The transport-modified spectral function and the calculated DC resistivity using this function are shown in Figure 2.6. The dashed curve in plot (a) shows the spectral function, while the dashed curve labelled (3) in plot (b) shows the calculated resistivity. In this case the parameters used for fitting are λ_0/ω_p^2 and the cutoff frequency for the ω^4 dependence.

These are found to be 0.0165 ± 0.0002 $1/\text{meV}^2$ and 24.0 ± 0.4 meV, respectively. Within the error ranges given, the difference between the calculated and experimental resistivities remains less than 0.05 $\mu\Omega$ cm for temperatures 0 to 200 K. Thus, the agreement with experiment is better over a larger range of temperatures than that of the delta function.

It is worth noting that the weight in the transport-modified spectral function above 40 meV is necessary for fitting the resistivity. Both the weight at low frequency and the characteristic frequency of the spectral function play a role in the low temperature curvature. While the low frequency weight may be removed by the transport-weighting, the absence of the weight at $\omega > 40$ meV reduces the characteristic frequency so that the upturn of the resistivity occurs at a lower temperature. This suggests that magnon excitations are contributing. On perhaps a more fundamental level, the value of $< \omega >$ for the transport-weighted spectrum is 45.1 meV, suggesting an average coupling of phonons <40 meV and magnons >40 meV.

Figure 2.7 shows a plot of λ as a function of temperature using the three spectral functions discussed. The vertical axis shows the mass renormalization in units of λ_0. Since we have only so far specified the ratio λ_0/ω_p^2, we cannot state λ in absolute units. All frequencies up to 1 THz are indistinguishable. Following the previous plots, the solid curve uses Gerasimenko's spectral function and the dashed curves use the alternative functions. Qualitatively, these curves are similar, the main difference being that the alternative functions display peaks. The dashed curve with the larger peak results from the delta spectral function.

This plot again demonstrates that the temperature dependence scales with the characteristic frequency $< \omega >=45$ meV=522 K. The consequence is that the full temperature dependence of λ cannot be detected without the heating of the sample to high temperatures. Currently, our experiment is only capable of around 320 K. The ratio of the room-temperature value to λ_0 is roughly 0.4. This ratio will serve as a criterion for the adjustment of certain input parameters to the THz-TDS calculations for Cr.
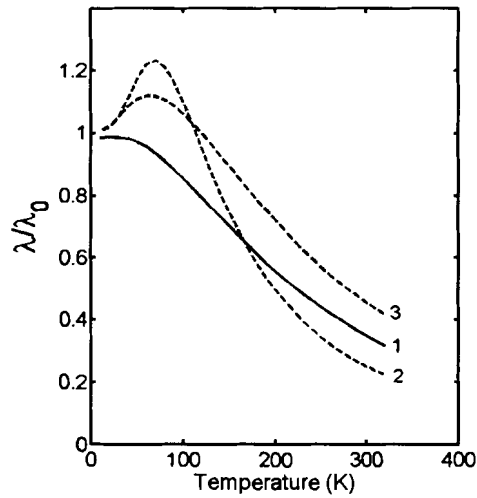
Figure 2.7: The quasiparticle mass renormalization in units of λ_0 as a function of temperature predicted for Cr using the three spectral functions discussed.

Chapter 3

Terahertz Time-Domain Spectroscopy (THz-TDS)

The electromagnetic spectrum has long been probed successfully through the infrared (10-789 THz) and microwave (10-100 GHz) frequencies. However, the overlap of these two ranges (0.1-10 THz) has been difficult to resolve, becoming known as the "THz Gap". This gap is an important frequency range for condensed matter physics. Scattering rates for carriers in semiconductors, high-temperature superconductors, and other strongly correlated electron materials lie in the THz. Also, energies of the superconducting gap in conventional superconductors and the donor and acceptor levels in semiconductors are matched by THz photons.

In the most basic sense, THz-TDS is an optical transmission or reflection experiment whose frequency range falls in the THz. The transmission setup was used for this work. Aside from the frequency range, what makes this spectroscopy powerful is that it is coherent. A gated detection method is employed, which enables the measurement of the electric field *amplitude* versus time, not its *intensity*. This allows the extraction of *phase* as well as amplitude information.

This chapter gives a brief introduction to the main aspects of the THz-TDS method. The reader is referred to reviews of the subject (e.g. Nuss and Orenstein [28]) for a full description. Following the experimental details, methods of extracting the important material parameters are discussed.
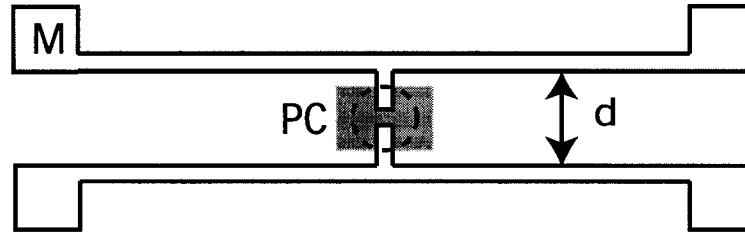
Figure 3.1: Schematic of the Auston switch used for the generation and detection of THz. The symbols indicate the metallic strip lines (M), the photoconductor (PC), and the effective dipole length (d).

3.1 Principles of THz Generation and Detection

The technique employed for the generation and detection of THz is based on the Auston switch [8][10]. A schematic of the switch is shown in Figure 3.1. It consists of two micro-fabricated metallic strip lines (M) separated by the length d. These strip lines are connected via the short vertical strip line sections and a photoconducting patch (PC). The square ends of the strip lines allow for electrical connection between any pair of leads. For current to run from one strip line to the other, a voltage bias must exist between the lines *and* photo-induced carriers must be excited in the PC. The dashed circle of Figure 3.1 indicates the desired laser spot for the optical excitation.

The switches used for generation (the "emitter") and detection (the "detector") are identical. The difference comes in what produces the voltage bias. We begin with the emitter. In this case, the strip lines are biased with an external voltage. We then optically excite carriers in the PC with an essentially instantaneous laser pulse, resulting in a short burst of photocurrent $J(t)$. The qualification of instantaneous is that the pulse is much shorter than the lifetime of the carriers. The carrier lifetime is controlled by implanting defects into the PC. The switch structure acts as a dipole of length d, so that the transient photocurrent radiates into free space like $E(t) \propto dJ(t)/dt$.

In the detector operation, the voltage bias is created by the THz pulse sent from the emitter. For clarity, a schematic of the detection is shown in Figure 3.2. The laser pulse and the THz pulse simultaneously strike the detector. The laser pulse excites carriers in the PC,
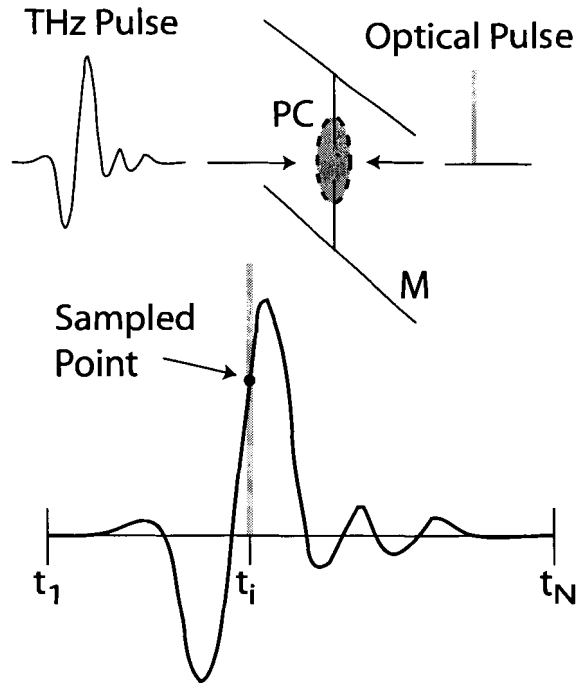
Figure 3.2: Schematic of the gated detection method.

while the THz pulse provides an electric field to drive the carriers. Since the laser pulse duration is much shorter than that of the THz, the laser pulse hits the PC instantaneously at time t_i while the THz pulse hits throughout the time interval $t_1...t_N$, where $t_1 < t_i < t_N$. The photocurrent induced is a convolution of the optical pulse and THz pulse sampled at the time t_i. By controlling the synchronization between the pulses, the sample time t_i can be adjusted within the range $t_1...t_N$. That is, the photocurrent corresponding to different points along the THz time trace can be measured, and the THz wave mapped out as a function of time.

The synchronization between the THz wave and the gating optical pulse is accomplished by using a single laser pulse to excite both the emitter and detector. A beam-splitter sends roughly half the pulse intensity to each antenna, while one of the pulses is sent through an adjustable time-delay stage. The time delay modifies the relation between t_i and the range $t_1...t_N$. The delay stage can be placed on either the detector or the emitter side. By adjusting the delay introduced, we effectively sweep the value of t_i through the range $t_1...t_N$, sampling
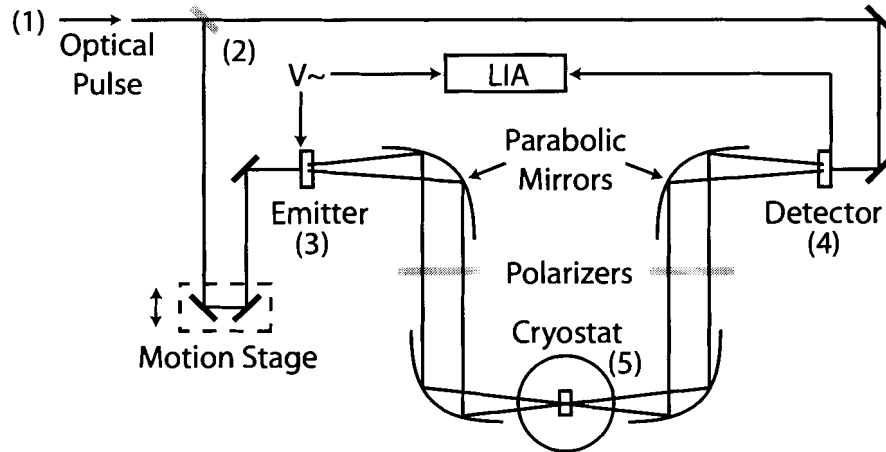
Figure 3.3: Schematic of the THz-TDS setup.

points along the THz wave.

3.2 Experimental Apparatus

Figure 3.3 shows a schematic of the apparatus. Optical pulses from an ultrafast laser (1) are beam-split at (2). One pulse is sent to the detector (4), while the other goes through a delay stage (motion stage) before it is sent to the emitter (3). A cone of THz radiation is generated by the emitter and collimated by an off-axis parabolic mirror. A second, identical mirror focuses the radiation through the sample which is located within the cryostat (5). The radiation transmitted through the sample is collimated and focused by two additional identical parabolic mirrors onto the detector. The emitter is given an AC voltage signal so that the photocurrent from the detector may be measured by a lock-in amplifier (LIA).

The ultrashort optical pulses are generated by a Kapteyn-Murnane Labs Kerr-lens mode-locked Ti:Sapphire laser. The Ti:Sapphire oscillator is pumped by a Spectra-Physics Millennia V Nd:YVO$_4$ laser. Quoting the original specifications from Kapteyn-Murnane, the pulses have a width in time of 15 fs, a bandwidth of 60 nm, a center wavelength of 800 nm, and a repetition rate of 80-90 MHz.

Though the laser pulse-width may be 15 fs immediately after the laser cavity, the subse-

quent path taken through air and glass introduces positive group velocity dispersion (GVD). This increases the pulse-width, since different frequency components have different velocities and thus a spatial dispersion. Pulse-broadening hinders the response of the emitter and lowers the resolution of the detector. Thus, an attempt is made to compensate by introducing optical elements which give negative GVD to the pulse. We have used either a prism compressor [35] or chirped mirrors for this purpose. The pulse-width at the antennas is estimated using a second-order intensity auto-correlation [14] to be 60 fs.

The PC material used for the Auston switches is silicon (100). Oxygen ions are implanted as defects to bring carrier lifetimes down to an estimated 0.6 ps. The substrate used is c-axis oriented sapphire and the metallic strip lines are aluminum. The dipole length is 50 μm, including the 5 μm gap which is patched by the PC. The resonance frequency of the dipole is roughly inversely proportional to the dipole length. The chosen dipole length yields a broad spectrum with its peak around 500 GHz. Longer dipole lengths yield narrower spectra which peak at lower frequencies.

Encapsulated within the emitter and detector components are a microscope objective lens, a substrate lens, and the antenna. The objective lens serves to focus the laser spot onto the PC patch, in order to maximize the number of photocarriers excited. The substrate lens serves to increase the coupling efficiency of the THz wave from the substrate to free space while increasing the collimation of the beam. An aplanatic hyper-hemispherical silicon lens was chosen with a radius of 5 mm and cut with a thickness of 5.962 mm. Including the sapphire thickness, the antenna is then located at the stigmatic point of the hyperhemisphere given by r(1+1/n).

The cryostat is a Janis Supertran VP 100 continuous flow liquid Helium cryostat. The sample is mounted on a movable vertical dip stick within the cryostat. Liquid helium is vaporized at the bottom of the chamber and the sample is surrounded by the helium vapor. Heaters and thermometers are mounted to the sample holder to accurately control and measure the temperature of the sample. This is done to an accuracy of 5 mK. The mount holds three samples of width 1 inch. In practice, the measurement of a single sample includes taking time traces through air, a reference, and the sample consecutively at each temperature. Thus the mount enables the measurement of two samples as long as they require the same reference.

The entire path of the THz beam is within a nitrogen-flushed enclosure. This is to avoid
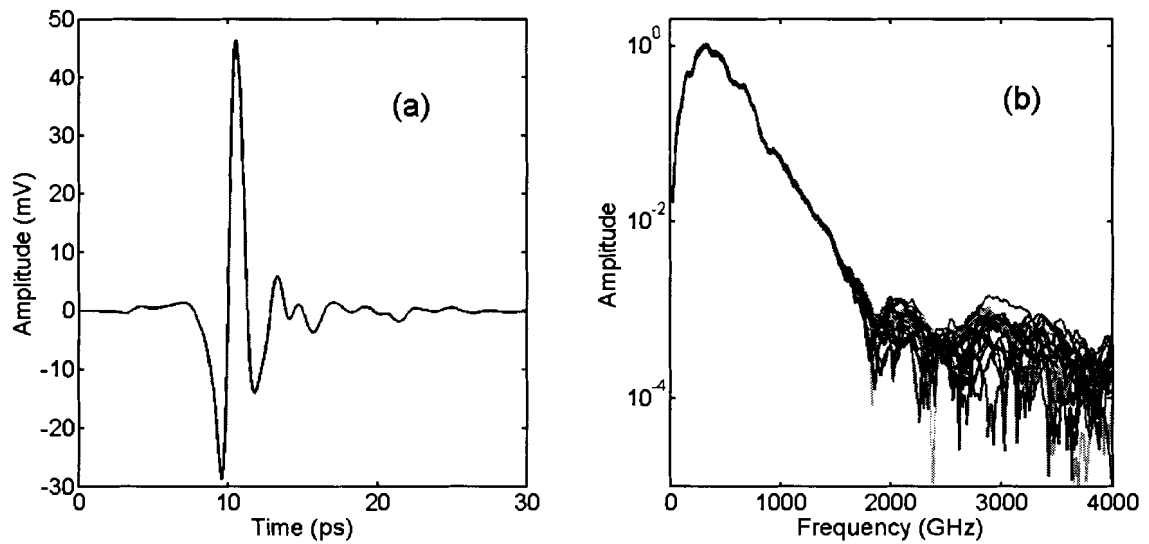
Figure 3.4: THz-TDS time trace through nitrogen-flushed air (a) and the FFT (b) of several such time traces.

the water absorption lines present when the beam travels through air. The absorption is caused by rotational excited states of the H_2O molecule. The dominant lines visible in our experiment are located at 557, 752, 988, 1097, 1163, and 1208 GHz [30].

An example time trace with no sample (air scan) is shown in Figure 3.4 (a). The vertical axis units of the time trace are millivolts while the time scale is in picoseconds (ps). Plot (b) shows the results of the Fourier transform of several such air scans. The amplitude has been normalized to its maximum and the frequency scale is in gigahertz (GHz). The experiment is most sensitive in the frequency range 300-800 GHz, where the THz spectrum has its maximum. Though the amplitude is still large below 300 GHz, these frequencies are corrupted by noise due to offsets in the voltage measured by the lock-in amplifier. Note that due to the time sampling being discrete and only over a limited range, the Fourier transform is accomplished via the fast Fourier transform (FFT).

Showing multiple spectra demonstrates that the signal above 2000 GHz is within the noise level. If we average this region of the spectrum, we find a signal to noise ratio of about 1400. If we take the peak of the noise oscillations as the noise level, the signal to

noise ratio reduces to about 1000. For a further understanding of the noise in the system, one must undertake a systematic study with a statistical sampling of time traces.

3.3   Extraction of Material Parameters

Transfer matrices provide the most general and succinct machinery for calculating the transmission of an electromagnetic plane wave through a series of stratified media (see Knittl [25]). The essential idea is to simultaneously solve the boundary conditions for the electric and magnetic fields at all the interfaces and account for the phase accumulated by passing through the layers. We can apply this formalism to THz-TDS by expressing the THz pulse as a superposition of plane waves. This is naturally accomplished using the Fourier transform. Due to the discrete time sampling of the THz pulses, a fast Fourier transform (FFT) algorithm is used. Transfer matrices provide the relation between the incident and transmitted pulses in the frequency domain in terms of material parameters of the sample such as the electrical conductivity.

The geometry under consideration is shown in Figure 3.5. Semi-infinite media exist on the far left and right of the structure, with indices of refraction n_0 and n_{k+1}. For our purposes, we take n_0 to be air and n_{k+1} to be the substrate. The substrate may be taken as semi-infinite since it is very thick and the optical field is pulsed. The time delay induced by travelling across the substrate is roughly equal to the pulse duration. Thus, reflections from the final substrate-air interface (not shown) will result in pulses which are separated in time. The time separation allows them to be windowed out. The adjustment in phase and amplitude due to the substrate thickness and the final substrate-air interface will be discussed later.

The structure itself consists of k films with corresponding indices of refraction n_k, which are, in general, complex and frequency dependent. The interfaces between the layers will be labelled by pairs $\{i|j\}$, such that the material on the left of the interface has an index n_i and the material on the right has n_j. The right and left going electric fields at the interface $\{i|j\}$ will be denoted by $E_{i|j,R}$, $E_{i|j,L}$, $E'_{i|j,R}$, and $E'_{i|j,L}$. The primed (unprimed) notation denotes the fields on the right (left) of the interface, while the subscripts R and L denote
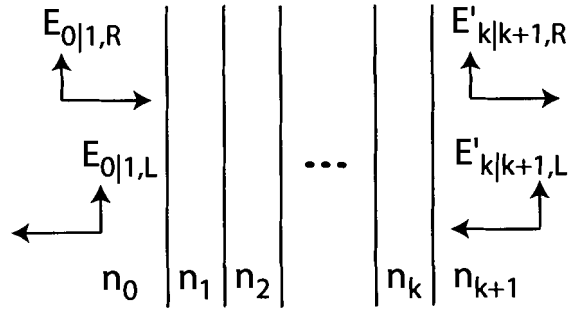
Figure 3.5: Geometry of k films surrounded by semi-infinite media with refractive indices n_0 and n_{k+1}.

right and left going fields. The system transfer matrix is defined by the relation

$$\begin{pmatrix} E_{0|1,R} \\ E_{0|1,L} \end{pmatrix} = S \begin{pmatrix} E'_{k|k+1,R} \\ E'_{k|k+1,L} \end{pmatrix} \tag{3.1}$$

The effect of each interface is included in a refraction matrix $W_{i|j}$ which represents the boundary conditions that the electric and magnetic fields must meet across the interface. We will only concern ourselves with normal incidence. The condition for continuity of the tangential components of the electric and magnetic fields can be written as

$$\begin{pmatrix} E_{i|j,R} \\ E_{i|j,L} \end{pmatrix} = W_{i|j} \begin{pmatrix} E'_{i|j,R} \\ E'_{i|j,L} \end{pmatrix} \tag{3.2}$$

where, the refraction matrix $W_{i|j}$ is given by

$$W_{i|j} = 1/t_{i|j} \begin{bmatrix} 1 & r_{i|j} \\ r_{i|j} & 1 \end{bmatrix} \tag{3.3}$$

Here $r_{i|j}$ and $t_{i|j}$ are the Fresnel reflection and transmission coefficients given by

$$r_{i|j} = \frac{n_j - n_i}{n_j + n_i} , \text{ and } \quad t_{i|j} = \frac{2n_j}{n_j + n_i} \tag{3.4}$$

Within each layer, the fields at opposing interfaces are related by the phase matrix U_j, given by

$$\begin{pmatrix} E'_{j-1|j,R} \\ E'_{j-1|j,L} \end{pmatrix} = \begin{bmatrix} \exp(-i\phi_j) & 0 \\ 0 & \exp(i\phi_j) \end{bmatrix} \begin{pmatrix} E_{j|j+1,R} \\ E_{j|j+1,L} \end{pmatrix} \tag{3.5}$$
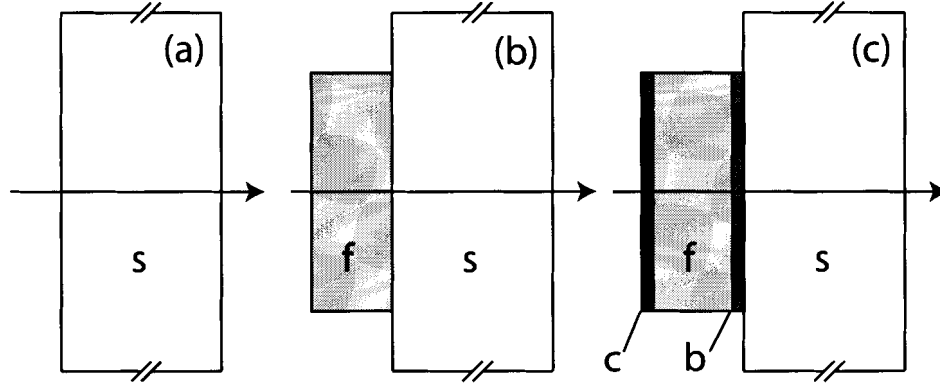
Figure 3.6: Geometries under consideration in the calculation of the transfer matrix in terms of the conductivity.

where $\phi_j = n_j d_j \omega/c$ is the phase accumulated across the layer. The indices $j-1$ and $j+1$ denote the layers to the left and right of layer j, respectively.

The system transfer matrix is now given by the product of refraction and phase matrices for all of the interfaces and layers. We have

$$\mathbf{S} = W_{0|1} U_1 W_{1|2} U_2 ... W_{k-1|k} U_k W_{k|k+1} \tag{3.6}$$

We shall apply this formalism to the film geometries shown in Figure 3.6.

3.3.1 Substrate

An analysis of the substrate is necessary to determine its index of refraction and whether it is suitable for measurement. Substrates must have a high transmission amplitude over the experimental frequency range. The index of refraction needs to be determined for later calculations since tabulated values are not always accurate or available at THz frequencies.

Following Figure 3.6 (a), we will calculate the transmission through a substrate in air. The solution for this simple case is obvious but serves to illustrate the transfer matrix method. Once again, taking the substrate to be semi-infinite, the transfer matrix is just the refraction matrix for the single substrate-air interface. Using Equation 3.3, we have

$$\begin{pmatrix} E_{a|s,R} \\ E_{a|s,L} \end{pmatrix} = 1/t_{a|s} \begin{bmatrix} 1 & r_{a|s} \\ r_{a|s} & 1 \end{bmatrix} \begin{pmatrix} E'_{a|s,R} \\ E'_{a|s,L} \end{pmatrix} \tag{3.7}$$

For a right-going pulse $E'_{a|s,L} = 0$, so that

$$\frac{E'_{a|s,R}}{E_{a|s,R}} = t_{a|s} = \frac{2n_s}{n_s + 1} \tag{3.8}$$

where n_s is the index of refraction of the substrate and the index of air is assumed to be unity.

The experimentally measured quantity is the electric field beyond the substrate-air $s|a$ interface (not included in Equation 3.7). The effect of travelling through the substrate is simply to introduce a phase $\phi_s = n_s d_s \omega / c$ and to reduce the amplitude by a factor $2/(n_s + 1)$. Denoting the measured field by E_m, we have

$$E_m = E_{a|s,R} \frac{4n_s}{(n_s + 1)^2} \exp(i\phi_s) \tag{3.9}$$

Note that any reflected waves from the substrate are being ignored by assuming the ability to window them out in the measurement of the THz pulse.

We can eliminate the field $E_{a|s,R}$ from the calculation by also measuring the field transmitted through a reference. The choice of the reference depends on the experimental quantity of interest. When studying the substrate alone, the reference is often a 'slab' of air. Including the phase accumulated by travelling through the air slab of thickness d_s and denoting the measured reference electric field as E_{ref}, we have

$$E_{ref} = E_{a|s,R} \exp\left(i\frac{d_s \omega}{c}\right) \tag{3.10}$$

We now define the experimental THz-TDS transfer coefficient as the ratio of E_m to E_{ref}. Thus, for our substrate analysis we have

$$t_{thz} = \frac{E_m}{E_{ref}} = \frac{4n_s}{(n_s + 1)^2} \exp\left(i\frac{(n_s - 1)d_s \omega}{c}\right) \tag{3.11}$$

If we choose our substrate to have negligible absorption (n_s is real), then the phase of the transmission allows the calculation of $d_s(n_s - 1)$. In making contact with the experiment, we must keep in mind that E_m and E_{ref} are the FFT of the experimentally measured THz pulses. Equivalently, they represent plane waves of frequency ω transmitted through the sample and reference, respectively.
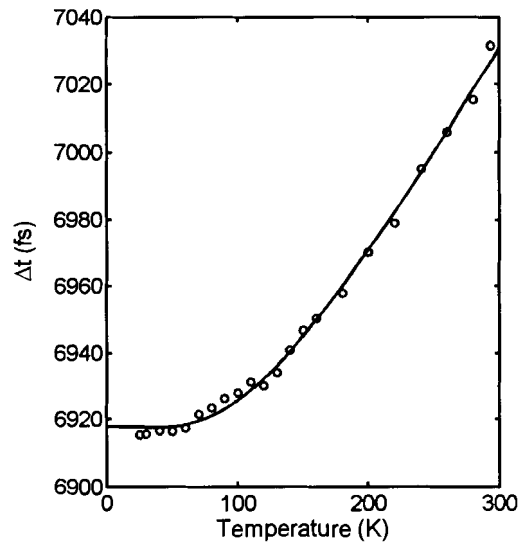
Figure 3.7: Phase slope of t_{thz} as a function of temperature for MgO.

The data points of Figure 3.7 show the slope of the phase of t_{thz} as a function of temperature for an MgO substrate, identical to those used for the chromium films. The frequency dependence (not shown) is small and has been averaged over the experiment's most sensitive frequency range 300-800 GHz. The temperature dependence is due to the contraction of the substrate as the temperature is lowered. This can be accounted for by fitting the phase slope with a phonon (Bose-Einstein) population function, shown as the solid line in Figure 3.7. We measure the thickness independently at room temperature and construct the temperature-dependent thickness. Thus, the total phase slope used for the calculation is about 7030 fs. If the substrate thickness is taken to be 0.977 mm = 3255 fs, then the index of refraction becomes 3.16. We can see that an accurate thickness is important for the correct index to be calculated.

Both the index of refraction and the thickness of a substrate can be extracted if one extends the scan length to include the twice-reflected pulse. The solid line of Figure 3.8 shows a room-temperature time trace through a sapphire substrate, as used for the Pb films. The first pulse has been directly transmitted through the sample, while the second pulse has undergone two reflections off the faces of the sapphire. These pulses can be windowed
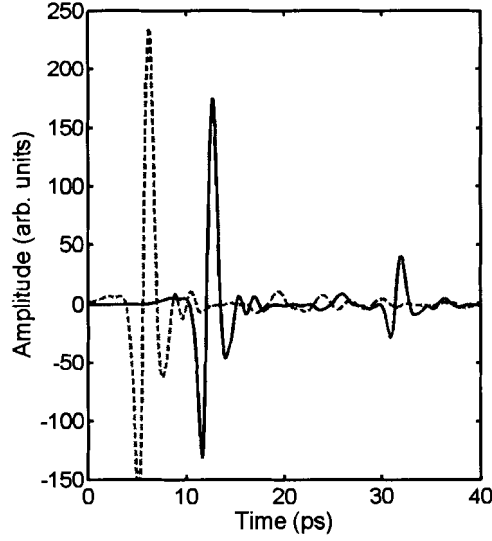
Figure 3.8: Time traces through air (dashed) and sapphire (solid), including the twice-reflected pulse through the sapphire which is useful for the calculation of n_s and d_s.

into two separate time traces, Fourier transformed, and compared in phase to the Fourier transform of an air-scan reference. The air-scan in the time domain is shown as the dashed line in Figure 3.8. The phase slope of the first sapphire pulse referenced to air is given by $(n_s - 1)d_s/c$, following Equation 3.11. The second sapphire pulse referenced to air has travelled through two extra sapphire thicknesses and thus has a phase slope of $(3n_s - 1)d_s/c$. Measuring these phase slopes allows us to calculate both n_s and d_s. For the sapphire substrates we find $n_s = 3.08$ and for the MgO we find $n_s = 3.16$. These agree with values found in Palik [31]. We shall use these values for later calculations.

3.3.2 Thin Film on Substrate

This is the most common sample geometry, shown in Figure 3.6 (b). The transfer matrix through the film is given by $\mathbf{S} = W_{a|f}U_fW_{f|s}$. This gives

$$\frac{E'_{f|s,R}}{E_{a|f,R}} = \frac{t_{a|f}t_{f|s}\exp(i\phi_f)}{1 + r_{a|f}r_{f|s}\exp(2i\phi_f)} \tag{3.12}$$

Once again, to obtain E_m we simply include the phase accumulated through the substrate and the reduction in amplitude due to the extra substrate-air interface.

It is useful to use an identical bare substrate as the reference in this case. This cancels the extra phase due to the substrate thickness and the Fresnel coefficient $t_{s|a}$. The extra terms that appear are the $t_{a|s}$ from the air-substrate interface and the phase from the air slab of thickness d_f. The THz-TDS transfer coefficient is then

$$t_{thz} = \frac{E_m}{E_{ref}} = \frac{t_{a|f}t_{f|s}}{t_{a|s}} \left(\frac{\exp(i\phi_f - i\omega d_f/c)}{1 + r_{a|f}r_{f|s}\exp(2i\phi_f)} \right) \tag{3.13}$$

Plugging in the explicit expressions for the Fresnel coefficients, this can be written as

$$\frac{1 + n_s}{t_{thz}} = \frac{e^{i\xi}}{n_f} \left[n_f(1 + n_s)\cos(n_f\xi) - i(n_f^2 + n_s)\sin(n_f\xi) \right] \tag{3.14}$$

where $\xi = \omega d_f/c$.

This equation can be numerically solved for $n_f(\omega)$. However, useful approximations are that $\xi n_f \ll 1$ and $1 < n_s \ll n_f$, which amounts to an optically thin film with a high conductivity. The former of these approximations will be discussed later in detail. Keeping only terms of order ξn_f from the Taylor expansions of $\sin(\xi n_f)$ and $\cos(\xi n_f)$, these approximations yield

$$\frac{n_s + 1}{t_{thz}} = n_s + 1 - i\xi n_f^2 \tag{3.15}$$

This is the most commonly used expression for the relation between the transmission and the complex index of refraction.

For nonmagnetic isotropic materials, the index of refraction relates to the dynamical electrical conductivity $\sigma(\omega)$ via

$$n^2(\omega) = 1 + \frac{i\sigma(\omega)}{\varepsilon_0\omega} \tag{3.16}$$

Equation 3.15 becomes

$$t_{thz} = \frac{n_s + 1}{n_s + 1 + Z_0 d_f \sigma(\omega)} \tag{3.17}$$

where Z_0 is the impedance of free space and the factor of unity was dropped from Equation 3.16 in accord with the approximation. Though chromium is magnetic, the magnetic

contribution to Equation 3.16 in our experimental frequency range (0.1-1.0 THz) is negligible (see Appendix B).

It was suggested that the reference be an *identical* bare substrate. Of course, in practice this is impossible. The indices of refraction may be identical but the thicknesses will not. This leads to an overall phase factor of $\omega(n_s - 1)\Delta/c$ in t_{thz}. The thickness difference Δ can be measured to about 1 μm using the methods described in the previous section. For sapphire ($n_s = 3.08$) this is equivalent to a phase slope of 7 fs. This accuracy is inadequate for the purpose of measuring extremely phase-sensitive quantities like λ. Thus, we must base the phase choice on other physically significant restrictions. The procedure for setting the phase is discussed when the experimental data is presented.

3.3.3 Thin Film Superlattice on Substrate

Due to the difficulties in preparing high-quality films of certain materials, more complicated geometries must be used, e.g. buffer and capping layers may be necessary. The lead films studied have buffer and capping layers of germanium and the chromium films have a capping layer of platinum. This section briefly describes the modifications necessary for these multilayer structures.

The geometry under consideration is shown in Figure 3.6 (c). Buffer and capping layers b and c have been added to the sample. The system transfer matrix is given by $S = W_{a|c}U_cW_{c|f}U_fW_{f|b}U_bW_{b|s}$. This yields a lengthy expression for $E'_{b|s,R}/E_{a|c,R}$ which is easy to derive with the previous definitions of $W_{i|j}$ and U_j. The reference used will be an identical bare substrate as it was for the single film geometry. The THz-TDS transfer coefficient is then given by

$$t_{thz} = \frac{E'_{b|s,R}}{E_{a|c,R}} \left(\frac{1}{t_{a|s}\exp\left(i(d_c + d_f + d_b)\omega/c\right)} \right) \qquad (3.18)$$

3.3.4 Approximation Analysis

The following addresses the approximation used to reach Equation 3.15. We find that this standard form has serious limitations which deserve attention.

The approximation in question is

$$\frac{\omega d_f}{c} n_f(\omega) \ll 1 \tag{3.19}$$

In any conductor, the index of refraction diverges at zero frequency. The manner in which it blows up will determine how good the approximation is. The simplest form to assume for n_f is the Drude model of Equation 2.6, which can be written as

$$n_f(\omega)^2 = i\frac{\omega_p^2}{\omega/\tau_0 - i\omega^2} \tag{3.20}$$

where ω_p is the plasma frequency and $1/\tau_0$ is the (frequency-independent) optical scattering rate. These quantities will play a key role in determining the validity of the approximation.

A more appropriate quantity to expand in powers of is $\omega d_f/c$, which is obviously small in the THz for films under 1000 Å. To perform an expansion in this quantity, it is useful to define some dimensionless parameters:

$$\alpha \equiv \frac{d_f}{c} 1/\tau_0 , \quad \beta \equiv \frac{d_f}{c}\omega_p , \quad \text{and} \quad \xi \equiv \frac{d_f}{c}\omega \tag{3.21}$$

Equation 3.20 can then be written

$$n_f(\xi)^2 = \frac{i\beta^2}{\xi\alpha - i\xi^2} \tag{3.22}$$

Our goal is to write the right side of Equation 3.14 as a Taylor series in ξ, assuming the ξ dependence of n_f in Equation 3.22. To first order, we have

$$\frac{n_s + 1}{t_{thz}} = n_s + 1 + \frac{beta^2}{\alpha} + i\xi\left[1 + \frac{\beta^2}{\alpha^2} + 1/2(1 - n_s)\frac{\beta^2}{\alpha} - 1/6\frac{\beta^4}{\alpha^2}\right] \tag{3.23}$$

For comparison, we expand Equation 3.15 in powers of ξ to first order and obtain

$$\frac{n_s + 1}{t_{thz}} = n_s + 1 + \frac{beta^2}{\alpha} + i\xi\left[\frac{\beta^2}{\alpha^2}\right] \tag{3.24}$$

The real parts of the two expansions are equal up to first order in ξ, while the slopes of the imaginary parts differ.

As can be seen by Equation 3.17, the same qualitative features should appear in the conductivity. That is, up to first order, the real part is well represented by the approximation while the slope of the imaginary part is not. The $\omega = 0$ Taylor expansion of the conductivity assuming the EDM form with a frequency-independent memory function is given by

$$\sigma = \frac{\omega_p^2 \varepsilon_0}{1/\tau - i\omega(1+\lambda)} \approx \omega_p^2 \varepsilon_0 \tau (1 + i\omega\tau(1+\lambda) + ...) \qquad (3.25)$$

Thus, a miscalculation of $\tau(1+\lambda)$ may result from the use of Equation 3.17. Since ω_p is usually chosen, while τ and λ are calculated, the quantity at risk here is λ.

We now attempt to obtain a quantitative estimate of the error in λ that occurs when the approximation of Equation 3.19 is used. For simplicity, we will assume values for all physical quantities and then calculate the exact THz-TDS transfer coefficient that would be measured. The approximate conductivity σ_{approx} can then be calculated using Equation 3.15 and compared to the exact conductivity.

The parameters of the model are ω_p, τ, λ, d_f, and n_s. Holding $\lambda = 1$ and $n_s = 3$, we observe how ranges of the remaining parameters effect the relative differences between the approximately calculated values of τ and λ and their exact values. The ranges considered are $100 < d_f < 400$, $3eV < \omega_p < 10eV$, and $1fs < \tau < 100fs$.

The relative error introduced in τ and λ is demonstrated in Figure 3.9 by plots as a function of the plasma frequency. For the τ error plot, the exact value of τ is set at 100 fs. Curves are shown for the thicknesses of 100, 200, 300, and 400 Å. The error is reduced for lower values of τ. For the λ error plot, the same thicknesses are shown with both $\tau = 1$ fs (thin) and 100 fs (thick). This plot shows that the primary terms which effect the validity of the approximation are the plasma frequency and the film thickness. The full range of the relaxation time does not play as strong of a role.

Obviously, the approximation is well justified for small thicknesses and low plasma frequencies. However, the lead films studied in this thesis lie in the thickness range 150-350 Å with a plasma frequency of 9.2 eV. Estimating from Figure 3.9, the extracted values of λ could be off by 30% if Equation 3.17 was used.
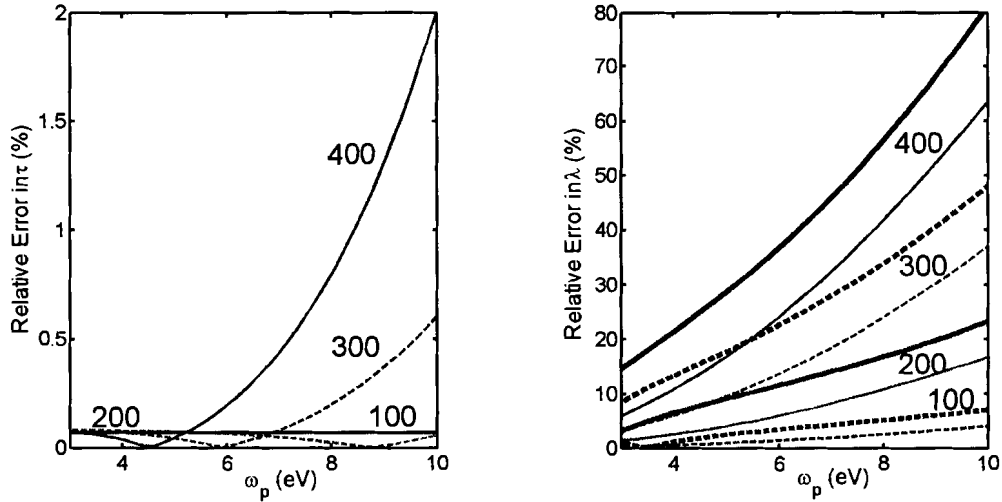
Figure 3.9: Relative error in τ and λ introduced by using the approximation of Equation 3.19 as a function of the plasma frequency. Thicknesses of d_f =100, 200, 300, and 400 Å are shown. The values of τ =1 and 100 fs are shown by the thick and thin curves in the λ plot while the τ plot shows only τ =100 fs.

3.3.5 Summary of Analysis Procedure

The calculations above describe how the electrical conductivity is extracted from the experimentally measured THz pulses. For clarity, we now review the procedure.

- THz time traces are measured through a sample and an appropriate reference.

- The THz transfer coefficient $t_{thz}(\omega)$ is defined as the ratio of the FFT of the sample time trace to the FFT of the reference time trace.

- The transfer matrix method enables the expression of $t_{thz}(\omega)$ in terms of the electrical conductivity $\sigma(\omega)$.

- Numerical computation yields $\sigma(\omega)$.

Chapter 4

Lead Films

In most instances, the production of high-quality samples is left to other research groups with relevant experience. In the case of lead, there were no readily accessible resources. Thus, the work was done by our group, which proved to be the most time-consuming part of the thesis. This chapter is meant to briefly outline this work and point out its successes and failures.

4.1   Growth Conditions

The lead films were grown in high-vacuum by thermal evaporation in the geometry shown in Figure 4.1. Buffer and capping layers of germanium form a sandwich-like structure around the lead layer. The substrates used were 10/5 polished c-axis sapphire discs of 0.615" diameter and 0.04" thick. The 10/5 refers to the scratch-dig parameters (10 μm scratch width and 50 μm dig diameter).

   The choice of this geometry stems from previous work growing thin films of lead [17][12]. It is shown that the tendency for lead to nucleate into islands can be combatted with the growth of germanium buffer and capping layers along with the cooling of the substrate during evaporation. The cooling reduces the thermal energy of lead atoms on the substrate surface, preventing subsequent migration after the initial collision. The cold substrate also serves to form an amorphous Ge buffer layer, which helps reduce strain between the Pb and its growth surface. The capping layer is primarily to prevent oxidation, since the experiment is not done *in situ* with the growth. However, it is also suggested [17] that
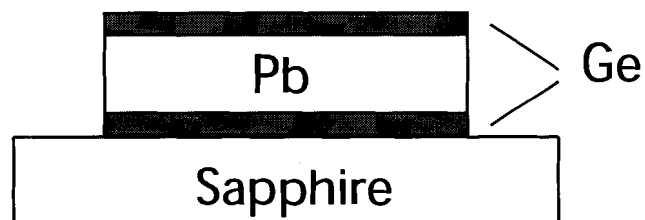
39

Figure 4.1: Film geometry for the lead films. Buffer and capping layers promote uniformity of the films and prevent oxidation when the film is transferred to the THz spectrometer.

this layer helps to prevent migration of the lead atoms when the sample is heated to room temperature.

The cooling of the substrate was accomplished by feeding copper tubing into the chamber, as shown in Figure 4.2. Liquid nitrogen (LN2) was run through this line in a continuous flow. A copper substrate holder is bolted to a copper plate which is soldered to the tubing. The thermal contact to the substrates is accomplished primarily by a thin copper sheet (cold finger) which is clamped to the copper holder and to the back of the substrates. The high thermal conductivity of sapphire makes certain that the heat on the growth face (front) of the substrate is lost to the nitrogen bath. The temperature of the substrates is believed to be close to that of LN2, although no attempt was made to measure the temperature directly. Certainly, the radiative heat from the boats is small in the high-vacuum environment.

4.2 Deposition Procedure

In the technique of thermal evaporation, the deposition material is heated within a high-vacuum chamber until a desired vapor pressure is achieved. In the case of lead and germanium, this is just past their melting points of 601 K and 1211 K, respectively. With the low pressure and high temperature, the vaporized atoms travel on (essentially) ballistic trajectories until contacting a surface of sufficiently low temperature to condense. The substrate and the walls of the bell jar usually qualify. The heating is accomplished by applying a high current through a thin metal sheet with a bowl-like indent (the boat), which the material is placed in. The rate of deposition is controlled by the amount of current put through the boat. Figure 4.2 indicates the copper risers that supply the current to the boats. The boats
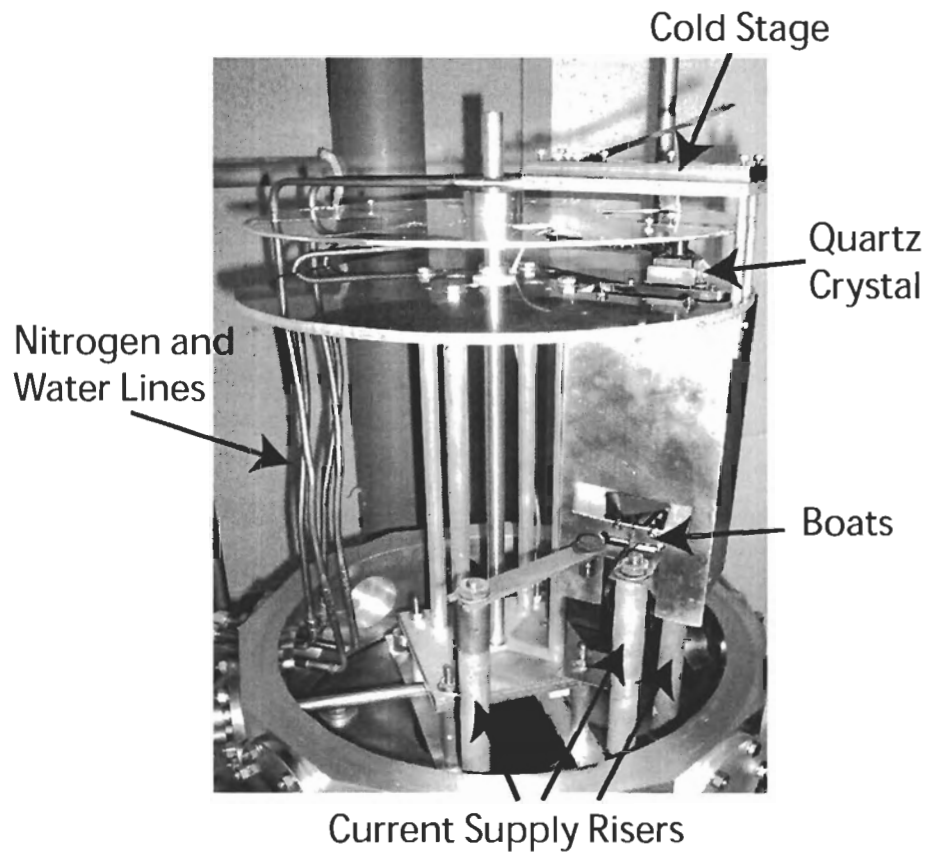
Figure 4.2: The evaporation chamber showing the cooling lines for the quartz crystal and the sample stage, the current source risers, and the boats.
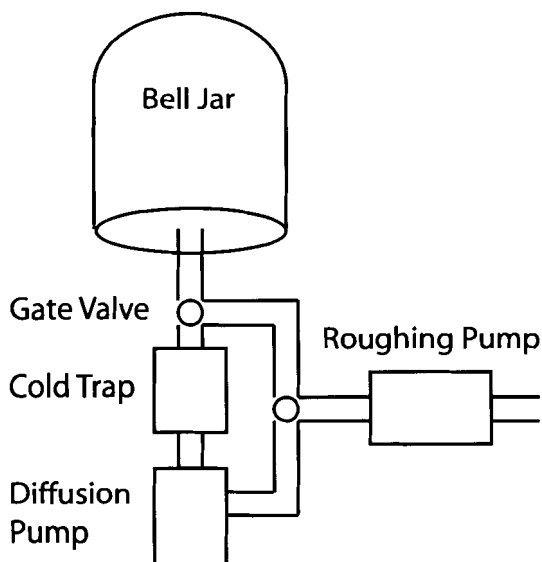
Figure 4.3: Schematic of the pumping system for the evaporator.

have been enclosed in an aluminum column to avoid deposition throughout the chamber.

The necessary high-vacuum environment is produced by the pumping system diagrammed in Figure 4.3. Three pumps are used; a mechanical (roughing), diffusion, and adsorption (cold trap). The mechanical pump is used to rough the chamber down to 50 mTorr. Once this pressure is reached, the pumping is switched to the diffusion pump line, which brings the pressure down to high vacuum levels. The cold trap serves as another pump in series with the diffusion and also to eliminate the backstreaming of oil from the diffusion and mechanical pumps to the chamber. The base pressure of this system is roughly 1×10^{-7} Torr. However, the cold sample stage and cooling lines provide additional cryo-pumping, bringing the pressure to roughly 8×10^{-8} Torr. The pre-evaporation of Pb and Ge greatly helped to bring the pressure down to these values. It also helps to reduce the oxygen content by forming the Pb-Oxide in the pre-evaporation instead of in the desired Pb film. During growth, the heat from the boats increases the pressure in the chamber slightly above these base pressures. The resulting pressure is about 3×10^{-7} Torr for Ge and 1×10^{-7} Torr for Pb.

The rate of deposition can be an important parameter for maximizing the film quality.

Some factors which determine the rate are the pressure in the bell jar, the temperature of the metal in the boat, the sticking coefficient to the substrate, and the geometrical configuration of the boat and the substrate. Our growth rates were monitored with the quartz crystal oscillator indicated in Figure 4.2. We estimate rates for the Pb growth to be 15 Å/s and those for Ge 1 Å/s. The Pb growth is done at a high rate to minimize the oxidation and to promote a continuous film.

4.3 Microscopy Studies

The need for the Ge layers and substrate cooling is supported by an analysis of the continuity of our films by Scanning Electron Microscopy (SEM). Figure 4.4 (a) shows an image of a Pb film grown at room temperature on sapphire with no Ge layers. The film is semi-continuous, with structure at roughly 0.5 μm. Figure 4.4 (b) shows a Pb film grown near LN2 temperature with a Ge buffer layer. The thickness of the Pb was not directly measured for these films but can reliably be estimated to be 20-60 nm. Film (b) is substantially more continuous with structure at a smaller scale. The lack of the capping layer may result in the remaining structure, according to the comment made earlier. Unfortunately, SEM studies done on the Ge-Pb-Ge structure were difficult since charge build-up on the 100 Å Ge capping layer impaired the imaging. However, the transient images seen showed no structure.

Atomic Force Microscopy (AFM) studies have been performed on Ge films and on the Ge-Pb-Ge structure in an attempt to analyze the continuity of the Pb film. The results are shown in Figure 4.5. Both the Ge and Ge-Pb-Ge films studied show an RMS roughness of about 9 Å with a peak-to-valley roughness of 100 Å. The lateral spacing of the roughness is on the scale of 0.5 μm. Since the identical surface structure is seen for the Ge films, we may hypothesize that the roughness present in the Ge-Pb-Ge multilayer is resulting from the Ge. A bare sapphire substrate was also measured, showing an RMS roughness of 2 Å and a peak roughness of 10 Å. Thus, there is no indication of an island structure in the Pb films.
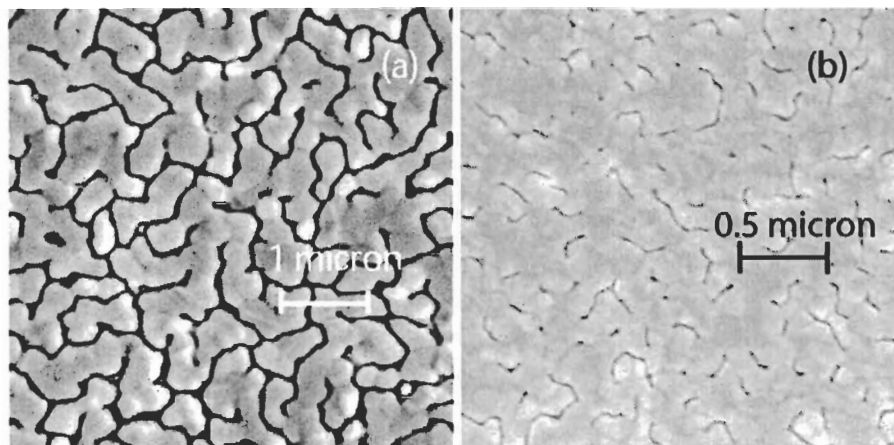
Figure 4.4: SEM images of Pb films. Plot (a) shows a Pb film evaporated at room temperature directly on sapphire and (b) shows a film grown with a cooled substrate and a buffer layer of Ge.

4.4 X-ray Diffraction

In order to determine the crystalline structure of the films and address the issue of lead oxidation, we have performed x-ray diffraction measurements. A CuK$_\alpha$ x-ray beam ($\lambda = 1.5418$ Å) was used with a diffractometer with an instrument resolution of $0.2°$. The instrument was calibrated with a $\Theta - 2\Theta$ scan of a single-crystalline c-axis sapphire substrate, identical to those used for the Pb-Ge-Pb films. The main sapphire peak was found at $2\Theta = 41.63°$, which is shifted from the standard value of $2\Theta = 41.71°$. Thus, the values of 2Θ given in the following analysis are shifted by $0.08°$.

Figure 4.6 shows the peaks found in $\Theta - 2\Theta$ scans of a Ge-Pb-Ge multilayer. To aid in the interpretation, the data points have been fit with Gaussian curves which seem to represent the peaks fairly well (better than Cauchy functions). The last two columns of Table 4.1 give a listing of the positions and intensities of these four peaks. The intensities are normalized to that of the largest peak at $31.33°$. The subscript 'exp' denotes these as experimental values.

In order to identify the peaks of Figure 4.6, we first calculate the peak positions for Pb assuming an fcc structure and a lattice constant of $a = 4.9508$ Å [16]. The peak relative intensities are then estimated using the inorganic chemical structure database (ICSD). The
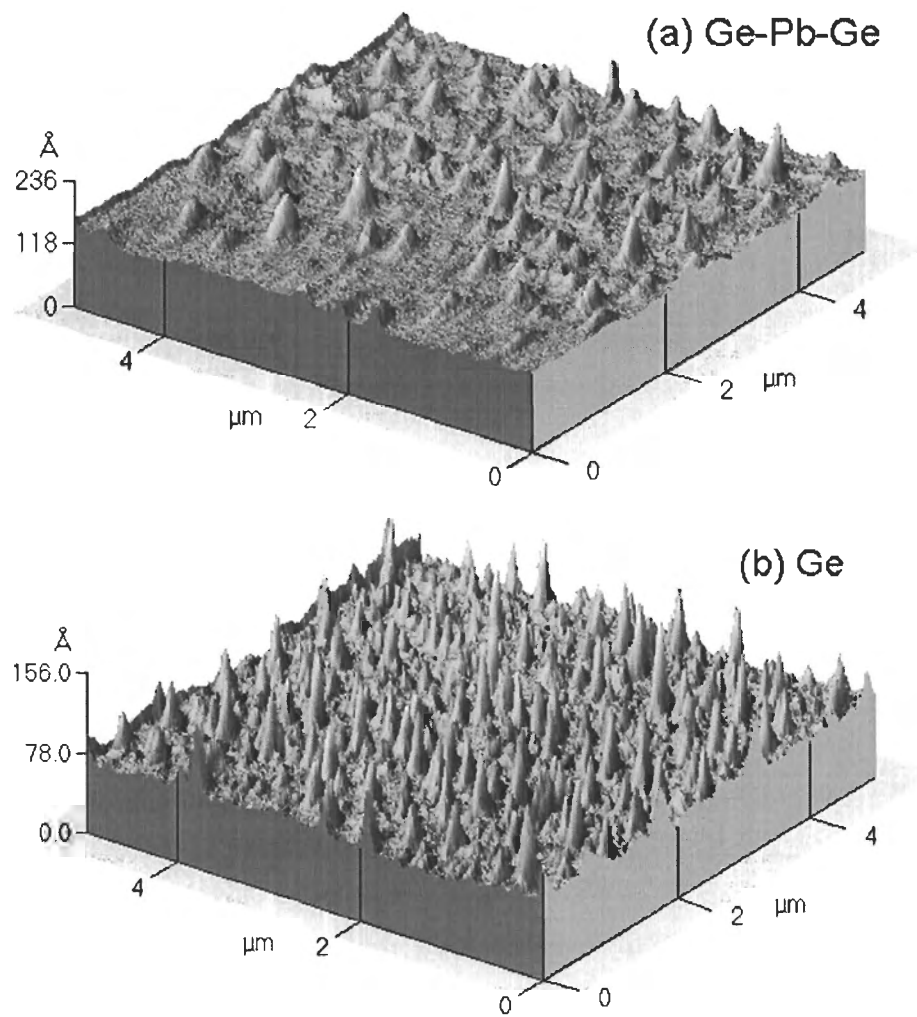
Figure 4.5: Plot (a) shows the top surface of a Ge-Pb-Ge (100-200-100 Å) structure while plot (b) shows the top surface of a Ge film (200 Å).
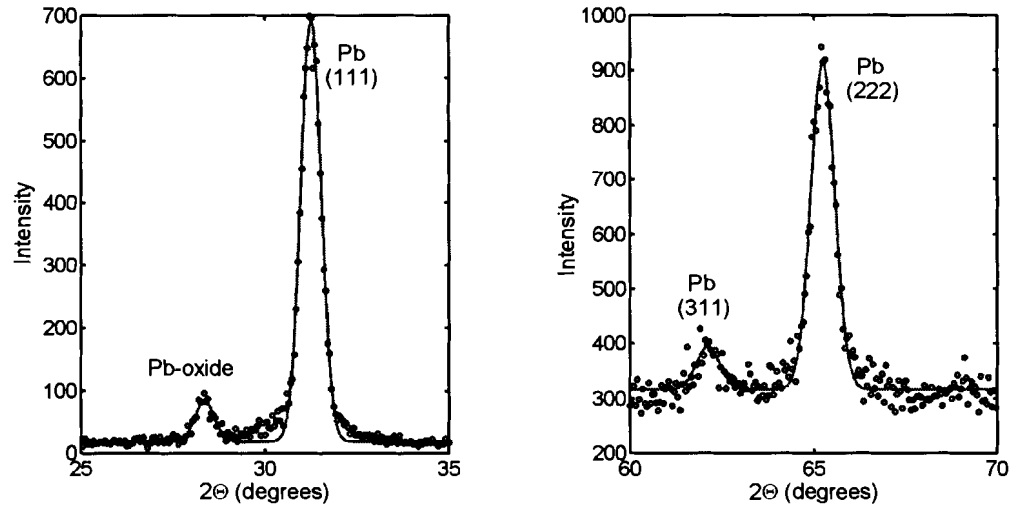
Figure 4.6: Peaks found from $\Theta - 2\Theta$ scans on the Ge-Pb-Ge multilayer. The intensity axes are in units of counts which are not related to each other.

Plane	2Θ	I/I_{max}	$(2\Theta)_{exp}$	$(I/I_{max})_{exp}$
Pb(111)	31.29°	1	31.33°	1
Pb(200)	36.29°	0.5	-	-
Pb(220)	52.26°	0.37	-	-
Pb(311)	62.19°	0.45	62.19°	0.007
Pb(222)	65.29°	0.13	65.32°	0.06
Pb-Oxide	28.39°	-	28.44°	0.1

Table 4.1: Description of X-ray diffraction $\Theta - 2\Theta$ peaks for Pb and Pb-oxide. Experimental 2Θ values and normalized intensities are compared to reference values (ICSD).

first three columns of Table 4.1 show the results. We interpret the three largest 2Θ peaks in Figure 4.6 as resulting from polycrstalline Pb. The experimental 2Θ values differ from the pure Pb reference values by less than the step size taken ($0.05°$). The difference in the relative intensities of the experimental peaks as compared to pure Pb and the absence of certain peaks is an indication of a preferential orientation. The large decrease in the intensity of the peaks from (200), (220), and (311), indicate that the percentage of crystallites with these orientations is small. The dominant orientation is (111) which also shows up in its harmonic at (222).

The peak in Figure 4.6 located at $28.44°$ has been identified as a Pb-oxide peak by comparison to the x-ray work of Venkataraj et al [19]. In a study of sputtered lead-oxide films, they detect the presence of four main oxides. The dominant peak is located at $28.39°$, and results from $PbO(101)$, $PbO_{1.44}(111)$, $Pb_2O_3(012)$, and $PbO_2(111)$. Which type of lead-oxide detected in our film is unknown and irrelevant to this study. Other peaks found by Venkataraj, are either much smaller than the $28.39°$ peaks or located in positions far from the peaks shown in Figure 4.6. The strength of the oxide peak is much less than the Pb(111) peak but slightly larger than the Pb(222). Since the relative intensities of the Pb-oxide and pure Pb powder peaks are unknown, we cannot predict the ratio of oxide to pure Pb.

No peaks were found which could result from the Ge layers. Assuming an fcc structure with a lattice constant of $a = 5.6575$ Å [38] and the ICSD, the peaks should be located at $27.3°$, $31.63°$, $53.7°$, $56.3°$, and $66.1°$. These positions are separated enough from the Pb and Pb-oxide peaks to be certain that they are not contributing. This implies that either the Ge is completely amorphous or the layers are too thin to create a reasonable diffraction intensity. As mentioned earlier, the cooling of the substrate during Ge growth should tend to form an amorphous structure.

The grain size of the Pb crystallites can be estimated using the FWHM values extracted from the Gaussian fits in Figure 4.6. The smaller the grain size, the broader the diffraction peak. Assuming cubic crystallites, Scherrer's equation [39] reads

$$B(2\Theta) = \frac{0.94\lambda}{L cos\Theta} \tag{4.1}$$

where $B(2\Theta)$ is the width of the peak (in radians), $\lambda = 1.5418$ Å is the x-ray wavelength, and L is the side length of the crystallite cube.

Before Equation 4.1 can be used, the broadening of the peak due to the instrument B_{instr} must be accounted for. To determine this, the peak for the (006) plane of sapphire was used. The FWHM determined from the Gaussian fit was $0.19°$. For Gaussian peaks, we have $B_{meas}^2 = B_{instr}^2 + B_{actual}^2$, while for Cauchy peaks $B_{meas} = B_{instr} + B_{actual}$ [39]. Equation 4.1 then gives grain sizes inferred from the Pb(111) and Pb(222) peaks of 135-145 Å for the Gaussian fit and 190-230 Å for the Cauchy fits. The value of 140 Å may be considered the most reliable since the peaks are best fit by the Gaussian form. However, the Cauchy fits suggest that this may be too low of an estimate. Similar grain size is found for the Pb-oxide crystallites, though that peak is not well resolved.

The important conclusion reached from the x-ray studies is that both Pb and Pb-oxide are present in the Ge-Pb-Ge multilayers. The ratio of the two cannot be determined with the information at hand. However, the thickness measurements of the following section will support a small percentage of oxidation. Subsidiary conclusions are that the Pb crystallites preferentially orient with the (111) plane parallel to the surface and have a grain size of roughly 140 Å. This grain size is less than but comparable to the thickness of the films (170-230 Å).

4.5 Thickness Measurement

The measurement of the thickness of the Pb layer in our films has been accomplished using two methods, the first mechanical and the second optical. The mechanical method was a profilometer, which uses a stylus tip to make contact with the sample. The stylus is dragged across a step edge where the film has been removed. We have made double step edges by scratching the film with a razor blade. This produces a surprisingly sharp edge for these films. The vertical displacement of the stylus tip indicates the thickness. Figure 4.7 shows example scans. Plot (a) shows the Ge-Pb-Ge structure thickness to be about 400 Å while plot (b) shows the Ge thickness to about 75 Å. If the total Ge thickness in both films is the same, we can infer a Pb thickness of 325 Å.

The other method used to measure the Pb thickness is to extract the D.C. resistivity $\rho(T)$ from the THz-TDS data. Since we do not measure the zero-frequency limit, we must extrapolate our data to zero frequency. As will be seen in the results chapter, $\Re(1/\sigma)$ is quite frequency independent so it may be fit over frequency to yield a reliable low-frequency
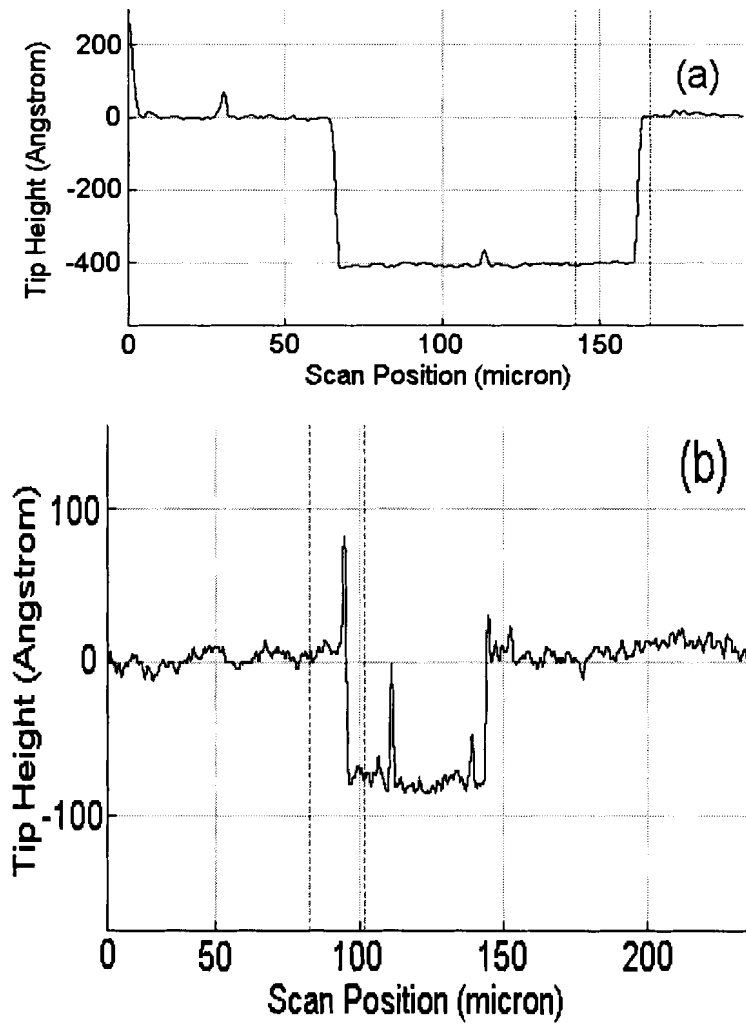
Figure 4.7: Example scans from the profilometer used to determine the thickness of the Pb films. The axes are stylus vertical position (nm) versus stylus horizontal position (μm). Plot (a) shows a scan on the full Ge-Pb-Ge structure while plot (b) is only the Ge.

limit. The determination of the thickness from $\rho(T)$ is based on the assumption that the scattering rate of the thin film differs from that of the bulk by a temperature independent term $1/\tau_{imp}$. This is certainly true for impurities and point-like defects. According to Matthiessen's rule [7], the contributing scattering rates add up, so that impurities and defects result in a shift in $\rho(T)$. If we assume our films to only differ from bulk lead by an impurity scattering rate, that is, the plasma frequencies are the same, then the slope of the measured resistivity must match that of bulk Pb. In order to obtain a thickness value with this method, one must adjust the thickness input parameter to the calculation until the desired $\rho(T)$ slope is obtained. The agreement of the resistivity slope method with the profilometer measurement is quite good (within 10%). The residual resistivities of our films range from 4-6 $\mu\Omega$ cm, indicating a reasonably low impurity content.

The agreement between thicknesses determined with the profilometer and resistivity method are indicative of little oxidation. We have observed that the lead-oxide formed is insulating in the THz. To determine this, lead films were grown on sapphire with no layers of germanium. The films were measured promptly after deposition and then again after being left open to the atmosphere. Figure 4.8 shows time traces through one of these samples. The dashed line indicates the scan directly after deposition and the solid line after three days in air. The rise in amplitude by a factor of about 2.8 signifies the same fractional increase in the resistivity. Thus, if the pure lead film had a room-temperature resistivity of 20 $\mu\Omega$ cm, then the oxidized film would have 56 $\mu\Omega$ cm. This means that the resistivity *slope* would be increased by the oxidation. Thus, the agreement between the two thickness measurements indicates little oxidation.

A more intuitive argument can be made regarding the thickness measurements and the oxidation issue. Let us say that either portions of the film are oxidized or there exists an isotropic oxidation of the film. When the optical transmission through the film is measured, the oxide will not contribute significantly to transport. Thus, the determination of the thickness would yield a smaller value, representing some effective thickness of the metallic fraction of the film. This amounts to a comparison of an *optical* thickness to a physical one, yielding the information regarding oxidation.
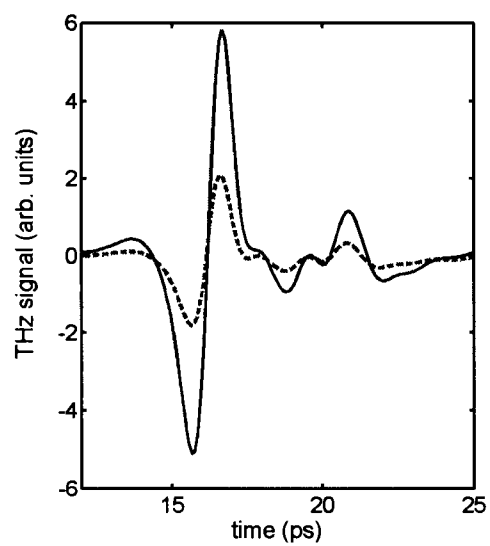
Figure 4.8: Time traces before (dashed) and after oxidation.

Chapter 5

Results

This chapter gives the final results of our experiment along with the physical interpretations of the data. Out of the many lead films studied, we focus on the two which display the highest quality data. We will refer to these as GePbGe-A and GePbGe-B. Results for these films are further supported by four other samples of lesser quality which display the same qualitative features. Following the analysis for lead, the results for two chromium films are discussed. For both lead and chromium, results will be compared to the theory discussed in Chapter 2.

5.1 Lead

The lead samples were grown in the Ge-Pb-Ge geometry and therefore the conductivity will be numerically solved from the t_{thz} data using Equation 3.18. In all the calculations, the Ge layers are taken to be identical with material parameters $d_{Ge} = 100$ Å and $n_{Ge} = 4.0 + 0.003i$ [31]. While the Ge thicknesses are not well-known, the absorption in the Ge is very small so that the thickness of the layers is unimportant. The sapphire substrate index of refraction is taken to be $n_s = 3.08$, in accordance with the substrate analysis discussed earlier. The thicknesses of the lead films in the GePbGe-A and GePbGe-B samples are 172 Å and 250 Å, respectively.

The results of the numerical calculation of $\sigma = \sigma_1 + i\sigma_2$ for GePbGe-A is shown in Figure 5.1. For clarity, only selected temperatures in the range 15 to 140 K are included. Data in the frequency range of 300-800 GHz is shown, where the THz spectrum has its
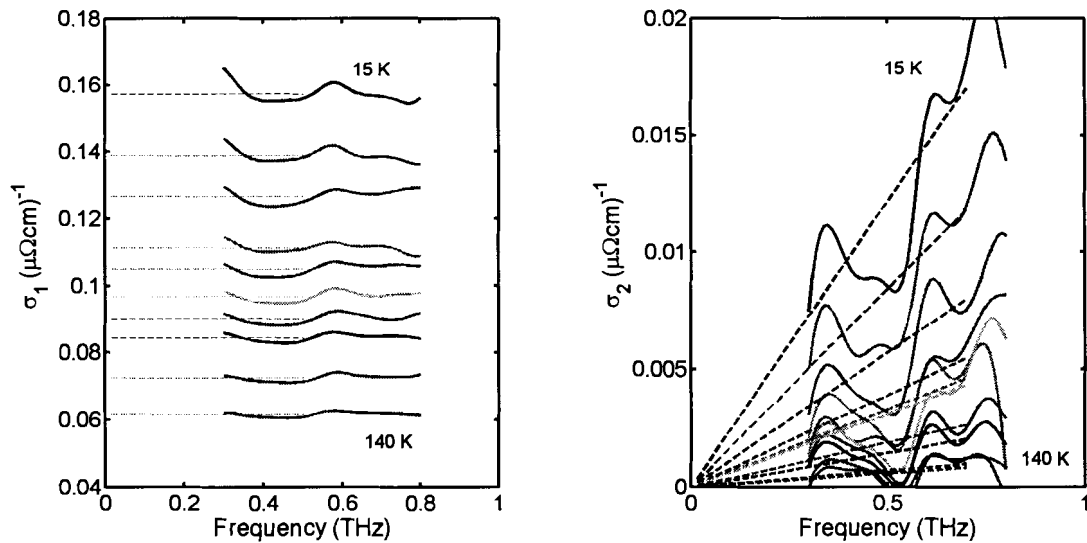
Figure 5.1: Plots of the complex conductivity as a function of frequency for GePbGe-A. Selected temperatures are shown in the range from 15 to 140 K.

maximum amplitude (see Figure 3.4). Even within this range, the data displays obvious oscillations. These result from noise in the time domain which, when Fourier transformed, becomes correlated. The appendix discusses the work in progress for an analysis procedure which decreases this effect.

For the time being, we must interpret the data by averaging over the oscillations. The dashed lines of Figure 5.1 indicate least-square fits over the useable frequency range. Following the expansion given in Equation 3.25, the real part is fit with a constant and the imaginary part is fit with a zero-intercept line. The rising σ_1 with decreasing temperature indicates the decrease in DC resistivity. The rise in the slope of σ_2 indicates an increase in the renormalized optical relaxation time $\tau^* = \tau(1 + \lambda)$. The corresponding plots for GePbGe-B are similar.

We now extract the DC resistivity $\rho(T)$. In the EDM, this is defined as the low-frequency limit of $\Re(1/\sigma)$. Figure 5.2 (a) shows $\Re(1/\sigma)$ for GePbGe-A as a function of frequency for a collection of temperatures in the range 15-290 K. The dashed lines indicate the fits over 300-800 GHz from which the DC resistivity is calculated. The weak frequency dependence makes these fits plausible. Once again, the corresponding plot for
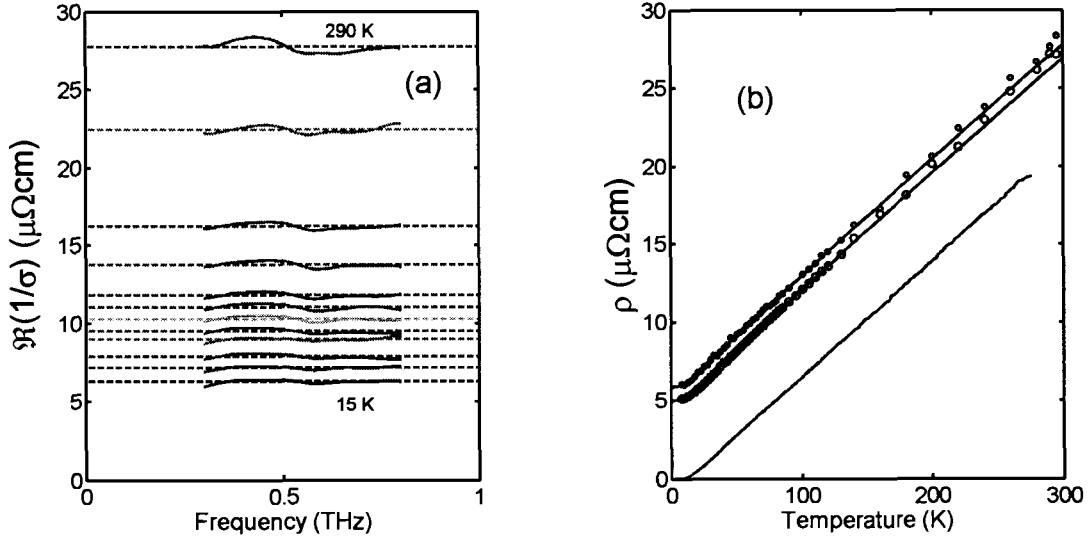
Figure 5.2: Plot (a) shows the real part of the inverse conductivity as a function of frequency for temperatures in the range 15-290 K. Plot (b) shows the extracted DC resistivities as a function of temperature.

GePbGe-B is similar.

The DC resistivity as a function of temperature for both GePbGe-A (small circles) and GePbGe-B (large circles) is shown in Figure 5.2 (b). Three solid curves are shown along with the experimental data points. The lowest curve is the bulk lead resistivity taken from the literature [1]. The curves going through the data points are the theoretical resistivity as shown in Figure 2.5 with appropriate residual resistivities added on according to Mattheissen's rule. These are 5.9 $\mu\Omega$ cm for GePbGe-A and 5.0 $\mu\Omega$ cm for GePbGe-B. As will be seen when τ^* and λ are calculated, the low temperature (<150 K) data more precisely describe the conductivity and therefore the higher temperatures are not included in this fitting.

As discussed in section 3.3.2, the uncertainty in the substrate thicknesses manifests itself as an unknown shift in the phase slope of t_{thz}. While the DC resistivity is insensitive to this shift, the calculation of λ requires that the phase slope be properly determined. We find that small adjustments in the phase slope leave the low temperature λ unaffected, while largely changing the high temperature value. Thus, the phase slope can be adjusted to yield the

appropriate high temperature value of λ. Due to the large noise present in λ, we must first average over frequency to obtain the temperature dependence. This is possible since both λ and τ are relatively frequency independent up to 1 THz (see Figure 2.3). The appropriate frequency range over which to average is best decided using the renormalized scattering time τ^*.

Figure 5.3 (a) and (b) show τ^* versus frequency for some temperatures in the range 15-140 K. Plot (a) is for GePbGe-A and plot (b) is for GePbGe-B. For GePbGe-A, the frequency range shown is 300-800 GHz while for GePbGe-B the range is 440-800 GHz. These ranges have been chosen by requiring that the slope of $\tau^*(T)$ has the same sign as predicted by theory. That is, a decrease in temperature should not result in a decrease in the scattering time. Though the plots show wild oscillations due to the Fourier transform effects, the data at fixed frequency has the appropriate temperature dependence. Outside the chosen frequency ranges, a variety of different temperature dependences are measured.

The result of the frequency averaging is shown in Figure 5.3 (c) and (d), which show the temperature dependence of τ^* for GePbGe-A and GePbGe-B, respectively. The fits over frequency include at least one full period of the oscillation to increase accuracy. The solid and dashed curves are the theoretical τ^* and τ, respectively. It is stressed that the only adjustment to the data in this plot is a shift in the phase slope of t_{thz}. Adjustment of this parameter by small amounts (± 5 fs) approximately shifts the τ^* curve. Thus, it is obvious that a renormalization is occurring since the data has too much curvature to fit the τ curve.

Now that a frequency range for averaging has been established, the phase slope of t_{thz} can be set using the high-temperature $\lambda \to 0$ requirement. Figure 5.4 (a) and (b) show the results of this procedure as compared to the prediction of theory (solid line).

Temperatures above 150 K have been excluded due to the noise. At these temperatures, it is difficult to achieve a precise measure of τ^* and λ. As can be seen from the low-frequency expansion of σ in Equation 3.25, the slope of σ_2 dominates the value of τ^*. At higher temperatures, σ_2 is small and the measurement has difficulty resolving it. For $1 + \lambda = \tau^*/\tau$, this is compounded with the decrease of the unrenormalized scattering time at high temperatures. The ratio of two small quantities results in a large experimental error. This does not pose a problem for this work since we are interested in temperatures where the renormalization is finite.

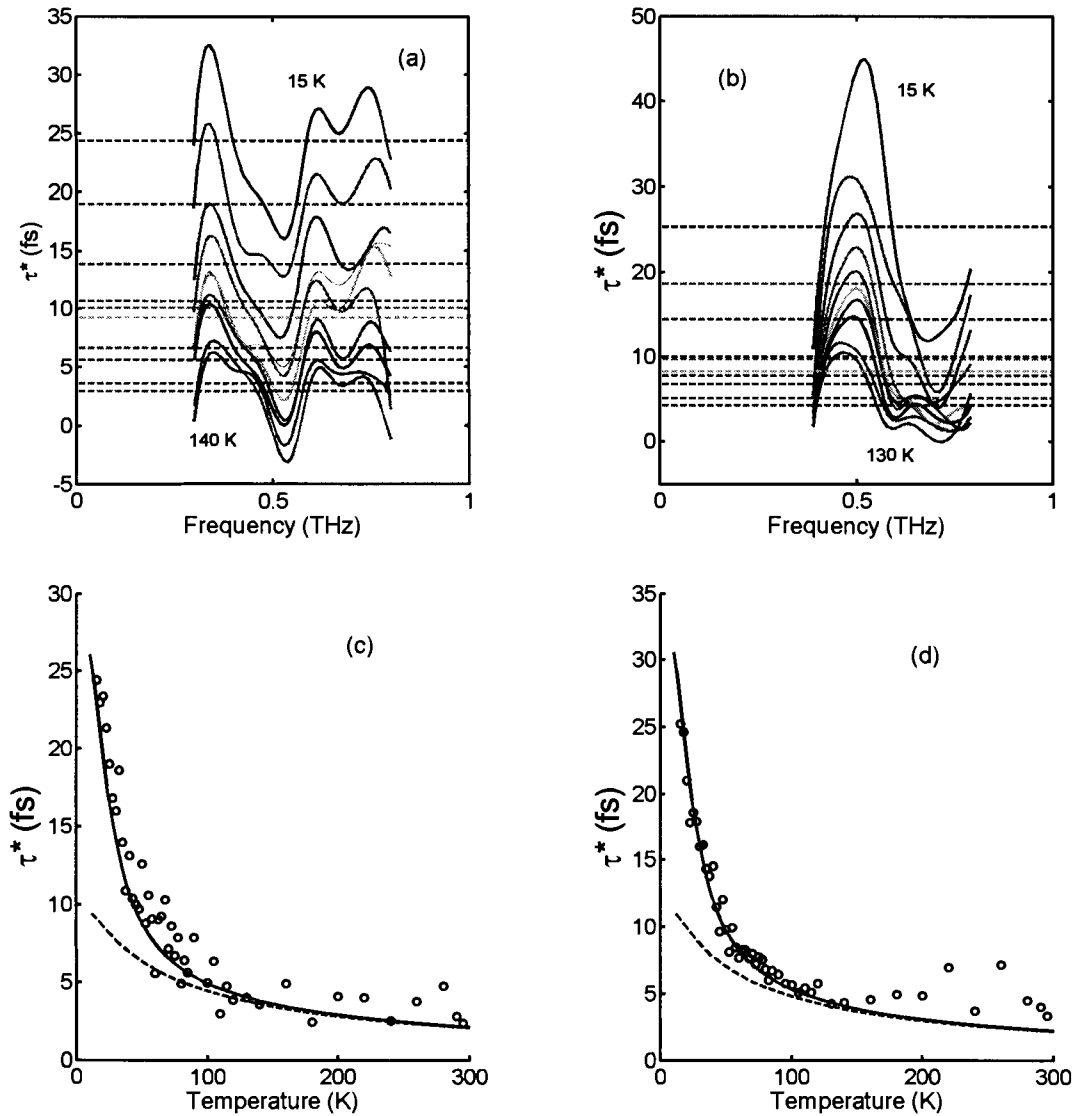Figure 5.3: Plots of τ^* as a function of frequency (a)(b) and temperature (c)(d). The dashed curves in plots (a) and (b) show the fits over frequency used to obtain the data points in plots (c) and (d), respectively. The solid and dashed curves in plots (c) and (d) show the theoretical τ^* and τ, respectively. Plots (a) and (c) are for GePbGe-A while (b) and (d) are for GePbGe-B.
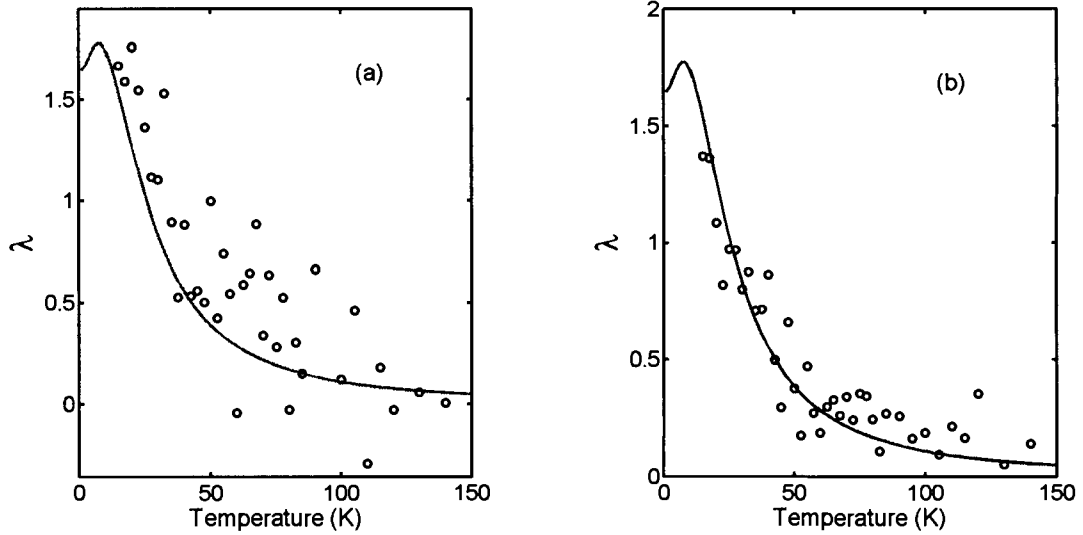
Figure 5.4: Quasiparticle mass renormalization as a function of temperature as compared with theory (solid line). Plot (a) shows GePbGe-A while plot (b) shows GePbGe-B.

We now perform the same analysis for the other Ge-Pb-Ge films. The residuals for these films range from 4.3 to 6.5 $\mu\Omega$ cm. Once again, the phase of t_{thz} is set by requiring that λ go to zero at high temperatures. Figure 5.5 shows λ as a function of temperature for four other films. The solid curves indicate the theory. For visual clarity, the plots are offset from each other by 2. Though the quality of data is obviously poorer, the agreement with theory is still apparent if not convincing.

The choices of the overall phase slope of t_{thz} and the frequency range to average over have been decided through physical requirements on λ and τ^*. However, we should try to understand the extent to which they influence the results for the mass renormalization. Within the frequency ranges chosen, the oscillations in frequency are coherent across different temperatures. Thus, the effect of changing the averaging range is to create a shift in λ. The shifts can be as dramatic as 0.5. However, this would make most of the data negative and therefore unphysical since λ reaches 0.5 around 50 K. The effect of the phase is to shift the high-temperature λ without changing the low-temperature value. Thus, the extrapolated λ_0 is not sensitive to the phase. For temperatures above 100 K, the mean amplitude of the scatter is greater than the effect of the uncertainty in phase.
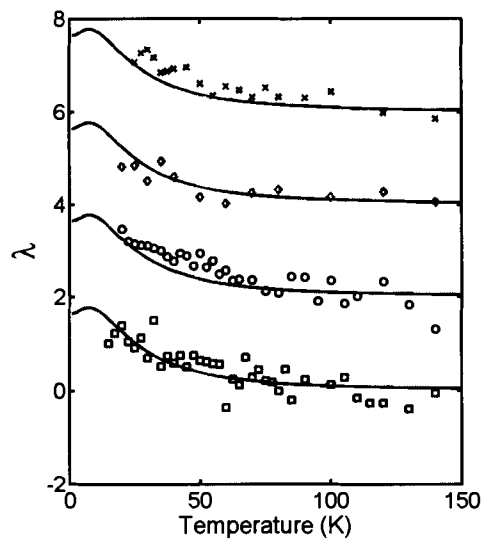
Figure 5.5: Quasiparticle mass renormalization as a function of temperature for four other Ge-Pb-Ge films. Data points are shown along with the theoretical prediction. Each data set is offset by 2 for visual clarity.

5.2 Chromium

This work is part of a larger work by Saeid Kamal and J. S. Dodge addressing the transport properties of Cr-V films. The Cr films were grown by sputtering by Eric Fullerton at Hitachi (San Jose CA, USA). The substrates chosen are MgO which has been measured to have $n_s = 3.16$ at THz frequencies. To prevent oxidation, a platinum capping layer was grown with a thickness of 10 Å. The reference is a bare MgO substrate. This two layer system can be solved with an equation similar to Equation 3.18. Though the conductivity of the capping layer of platinum is not well known, it has been found to play a negligible role in our results. Thus, the index of refraction of the platinum is taken to be the same as that of Cr. The THz-TDS data for two films will be shown. These films have Cr thicknesses of 345 Å and 358 Å.

We note that Equation 3.16 is used to express the index of refraction in terms of the conductivity. Thus, the magnetic contributions present in chromium are neglected. Appendix B discusses this approximation.

The resistivity as a function of temperature is shown in Figure 5.6. The data points are from fits of $\Re(1/\sigma)$ over 400-800 GHz. The solid line shows the DC resistivity curve for bulk Cr [6]. The kink in the resistivity due to the antiferromagnetic transition appears at a temperature of around 300 K for the THz-TDS data.

The dashed line in Figure 5.6 indicates the model discussed in chapter 2, using the transport-weighted version of Gerasimenko's spectral function. A residual resistivity of 2.06 $\mu\Omega$ cm was included according to Mattheissen's rule. The THz-TDS data is slightly different from the bulk Cr data and thus, the fit is not nearly as good.

We now move to extract the quantities of interest. As in the case of Pb, the overall phase slope of t_{thz} must be set by conditions on the high-temperature λ behavior. In chapter 2, we found that the energy scale determined by Gerasimenko's spectral function results in the property that $\lambda(300\ K)/\lambda_0 \approx 0.4$. This can be used to set the phase slope in the same manner that $\lambda \rightarrow 0$ at high temperatures was applied for Pb.

Once again, before the phase is exactly set, the range of frequencies to average λ over is decided by requiring the appropriate temperature dependence of τ^*. Figure 5.7 shows τ^* as a function of frequency for a few temperatures within 15-320 K. The range 400-700 GHz satisfies the criterion that the sign of the slope of $\tau^*(T)$ agrees with the theory. In this
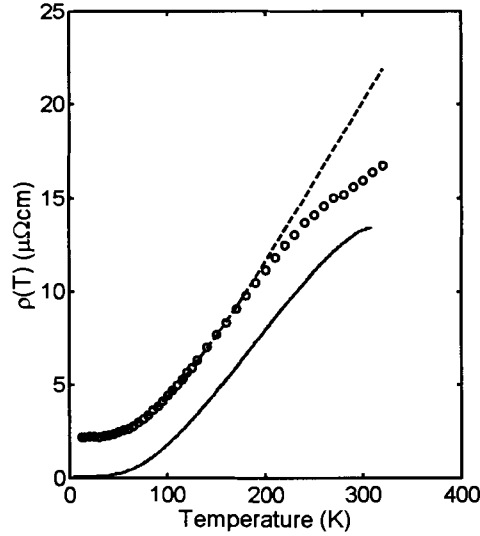
Figure 5.6: DC resistivity as a function of temperature for Cr. The solid line indicates the bulk Cr curve and the dashed line shows the model.

case, $\tau^*(T)$ actually changes to a slightly positive slope at the lower temperatures due to the peak in λ. Thus, the criterion that τ^* decrease with increasing temperature is applied to temperatures above 50 K.

For Cr, only the ratio of λ_0/ω_p^2 is known from the theoretical resistivity, so that we must find an appropriate procedure for consistently determining the overall phase and the values of λ_0 and ω_p. This can be done using only the experimental $\lambda(T)$ data. Firstly, the overall phase factor is adjusted to maintain $\lambda(300~K)/\lambda(0~K) \approx 0.4$, where $\lambda(0~K)$ is estimated by the extrapolation of the experimental λ to zero temperature. Then the value of ω_p is adjusted until $\lambda(0~K)/\omega_p^2$ matches the value determined previously by the theoretical resistivity of Figure 5.6.

The results are shown in Figure 5.8 for two films studied. Plots (a) and (c) show τ^* as a function of temperature while plots (b) and (d) show λ as a function of temperature. The results of the calculation for the two films studied are very similar. The film represented in plots (a) and (b) has $\omega_p = 3.6$ eV and $\lambda_0 = 0.21$, while the film represented in plots (c) and (d) has $\omega_p = 3.5$ eV and $\lambda_0 = 0.20$. In both cases, the data shows a peak in $\lambda(T)$ which was not predicted with the use of Gerasimenko's spectral function. The error range for the
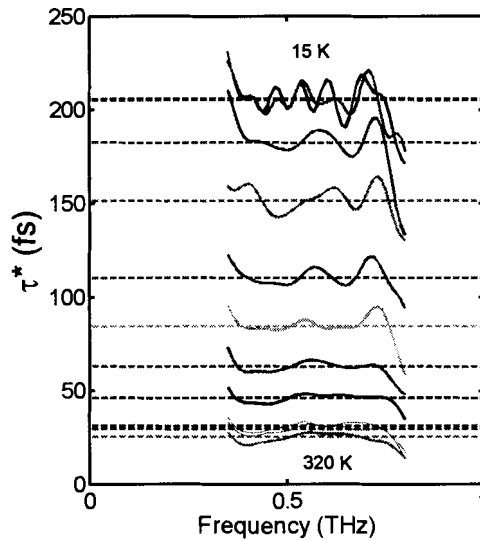
Figure 5.7: Renormalized scattering time as a function of frequency for a few temperatures in the range 15-320 K.

value of λ_0 may be estimated to be ± 0.05, which is equal to the standard deviation of the difference between the experiment and theory.

As we did for Pb, we should try to understand the extent to which the choice of the averaging frequency range and the overall phase of t_{thz} influence the results for the mass renormalization. In this case, the amplitude of the oscillations in frequency is much less. Thus, changes in the averaging frequency range result in shifts of less than 0.05. Since the value of λ_0 is smaller, the percentage shift is similar to that of Pb. The effect of the overall phase slope factor is greater for Cr than it was for Pb. This is because the renormalization is still occurring at high temperatures, where changes in the phase slope result in large changes in λ. The requirement of the theoretical ratio of $\lambda(300\,K)$ to $\lambda(0\,K)$ is paramount to reaching the results shown for $\lambda(T)$. Again, this ratio should be reliable since it is primarily due to the characteristic energy scale of the spectral function determined by Gerasimenko *et al.*
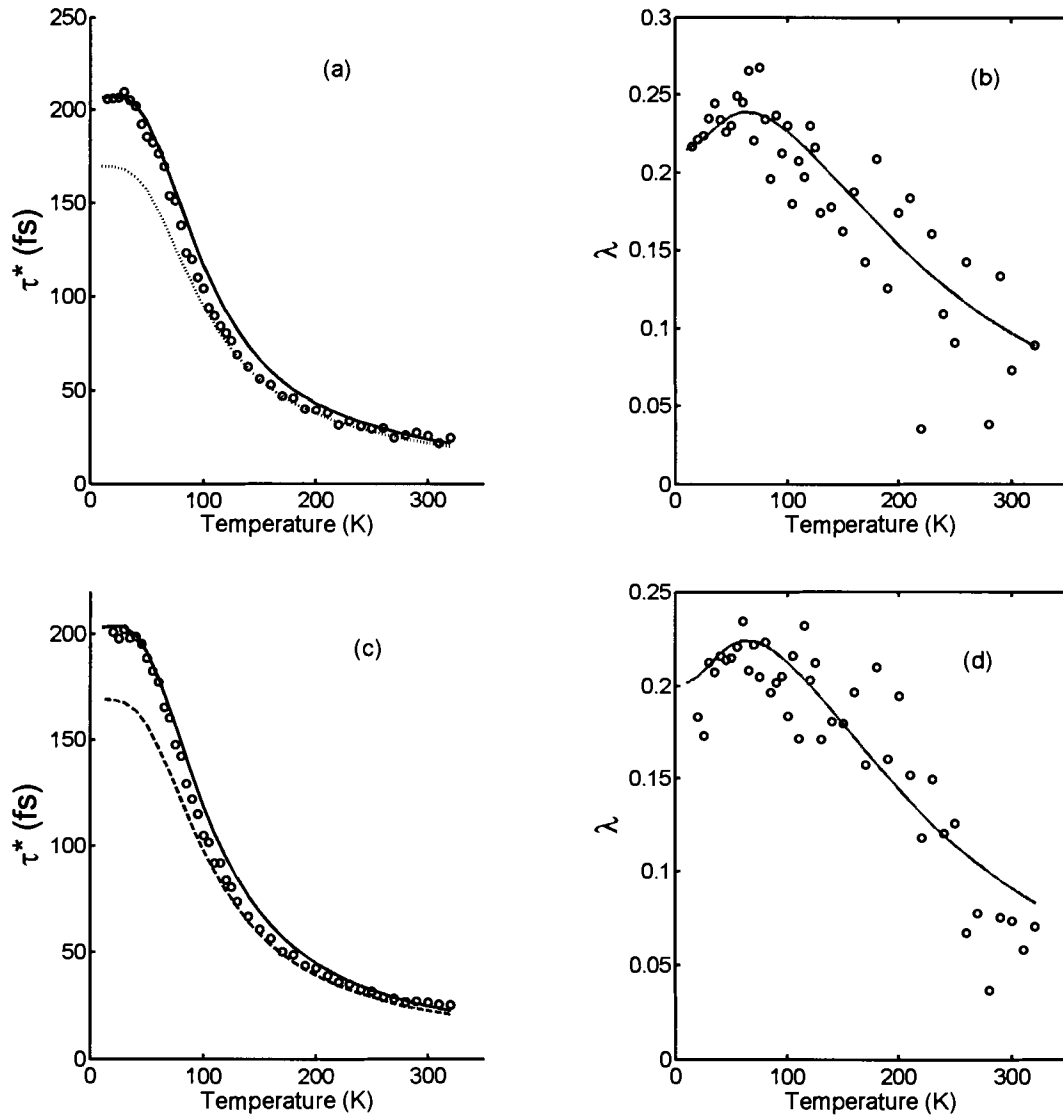
Figure 5.8: Plots (a) and (b) show $\tau^*(T)$ and $\lambda(T)$ for one Cr sample, while plots (c) and (d) show the same for a second Cr sample.

5.3 Conclusions

The optical conductivity of lead and chromium in the frequency range of 300-800 GHz has been measured using THz-TDS. The results demonstrate that the quasiparticle mass renormalization factor $\lambda(\omega, T)$ of the EDM can be measured in these materials. The frequency dependence below 1 THz is weak so that an accurate measurement of the temperature dependence in the range 0-300 K can be obtained by averaging over frequency. This is to be contrasted with specific heat and electron tunnelling experiments which only measure the low-temperature value λ_0.

In the case of lead, the agreement with the theoretical treatment considered is quite good. Firstly, this demonstrates that the weak-coupling approximation used to derive the memory function of Equation 2.13 is valid even for a strong-coupling conventional superconductor. Secondly, this points to the validity of replacing the transport-weighted Eliashberg spectral function with the isotropically-weighted version derived from electron tunnelling measurements.

The agreement of the experiment with theory suffers in the case of chromium mostly due to an incomplete study of the bosonic spectral function. We have seen that the spectral function determined by Gerasimenko *et al* needs modification in order for the theory to yield the proper curvature in the DC resistivity. Furthermore, the use of this spectral function does not predict the peak in $\lambda(T)$ shown by this experiment. We have demonstrated that the application of a transport-weighting procedure which reduces the spectral function weight at low frequency yields an improved agreement with experiment. The value of λ_0 is found to be 0.21 ± 0.05, which sets the amplitude of Gerasimenko's spectral function.

Future work on the nonlinear-optic generation of THz may permit the measurement of the frequency dependence of the memory function by extending our experimental frequency range up to energies commensurate with the bosonic excitations. However, the temperature dependence of the memory function has proved to be an effective probe of the electron-boson coupling. The temperature scales of the memory function and the DC resistivity correspond to the frequency scales of the bosonic spectral function. Details in the curvature of these quantities with temperature can indicate the finer structure in the spectral function.

Appendix A

Data Analysis

An inherent difficulty in THz-TDS is moving from the time domain, where the measured quantity lives, to the frequency domain, where the important transport quantities are defined. The difficulty arises from measuring only a finite time interval. When fast Fourier transformed, this windowing creates undesirable oscillations in the frequency domain. This section will discuss the prospects of an analysis method designed to remedy this problem.

The adverse effects of the FFT become greater when the signal to noise ratio is reduced. The signal to noise ratio is considerably worse for the sample scans than for the reference scans. Thus, it may be reasonable to only avoid taking the FFT of the sample time trace. This can be done with the following procedure.

The measured quantities are the reference time trace $E_r(t)$ and the sample time trace $E_s(t)$. The reference is directly Fourier transformed to obtain $E_r(\omega)$. The transmission $T(\omega)$ is expressed in terms of a parameterized conductivity $\sigma_{\{c\}}(\omega)$, where $\{c\} = \{c_0, c_1, ...c_j, ...c_N\}$ is the set of coefficients in the Taylor expansion of $\sigma(\omega)$ about $\omega = 0$. Since $\sigma(\omega)$ is causal, we must have $\sigma(\omega) = \sigma(-\omega)^*$. Thus, we write the expansion as

$$\sigma_{\{c\}}(\omega) = \sum_{j=0}^{N} i^j c_j \omega^j \tag{A.1}$$

Note that performing the expansion about $\omega = 0$ and using the factor i^j ensures that the coefficients are real. The sample time trace is now fit in a least squares sense by varying $\{c\}$ in the relation

$$E_s(t) = \text{ifft}(T_{\{c\}}(\omega)E_r(\omega)) \tag{A.2}$$

64

where ifft(x) represents the inverse fast Fourier transform operation performed on the quantity x. This method of analysis will be referred to as the temporal σ-fit (TSF) method.

In order to understand the advantages and disadvantages of this analysis, we will invent a theoretical $E_r(t)$ and $\sigma_{th}(\omega)$ and perform the analysis to extract out $\sigma_{ex}(\omega)$. The conductivity $\sigma_{th}(\omega)$ is taken to be Equation 2.16, with frequency independent values of $\tau = 10$ fs, $\lambda = 1$, and $\omega_p = 9$eV, which are appropriate for lead. From $\sigma_{th}(\omega)$, the theoretical transmission $T(\omega)$ is calculated via Equation 3.15, for simplicity.

The reference time trace $E_r(t)$ is defined to be a tenth order Hermite function, whose parameters are determined by least-square fitting to a typical reference scan. Figure A.1 shows the fit of $E_r(t)$ to a typical experimental reference scan. The curve with more wiggles is the experimental data. The sample time trace is now given by $E_s(t) = E_r(\omega)T(\omega)$. $E_s(t)$ is almost identical to $E_r(t)$ but reduced in amplitude. If the analysis was now performed the agreement between the extracted parameters would be extremely good. However, the appropriate test of the procedure lies in its ability to treat experimental noise. Thus, we now add a noise floor to both $E_s(t)$ and $E_r(t)$. The signal to noise ratio for the spectrum of $E_s(t)$ is taken to be about 10^3, which is more than our experiment usually provides but serves to illustrate this analysis method.

We will expand the conductivity up to fifth order in frequency (ω^5) so that $\{c\}$ consists of six terms. An initial rough comparison can be seen in Figure A.2, which shows the real and imaginary parts of the conductivity in panels (a) and (b) respectively. Three curves are shown; the theoretical, the direct FFT calculation, and the TSF calculation. This plot suggests that the TSF method has some merit but is far from a conclusive study.

A statistical analysis can be achieved by generating many sets of random noise and performing the calculation of $\sigma(\omega)$ for each set. Example histograms at 500 GHz for the real and imaginary parts of the conductivity are shown in Figure A.3. The vertical axes are counts which is related to the statistical sample size and the number of bins. Data for the direct FFT and TSF calculations (shown as circles) have been fit with Gaussian curves, the dashed showing the FFT and the solid showing the TSF. The vertical solid lines indicate the exact (theoretical) values. The Gaussian fits enable the extraction of two important quantities; the center value and the width of the distribution. We can see that the real and imaginary parts show small or no shifts in the center value for both FFT and TSF calculations, while the width of distributions are greatly reduced with the TSF method.
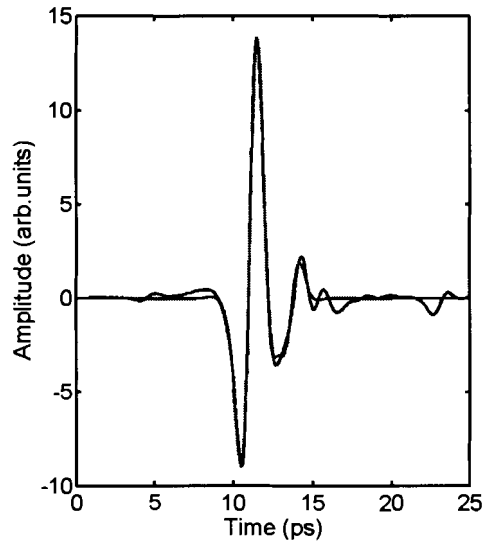
Figure A.1: Time traces of the experimental reference scan and the theoretical reference scan generated by fitting a Hermite function to the experimental curve.
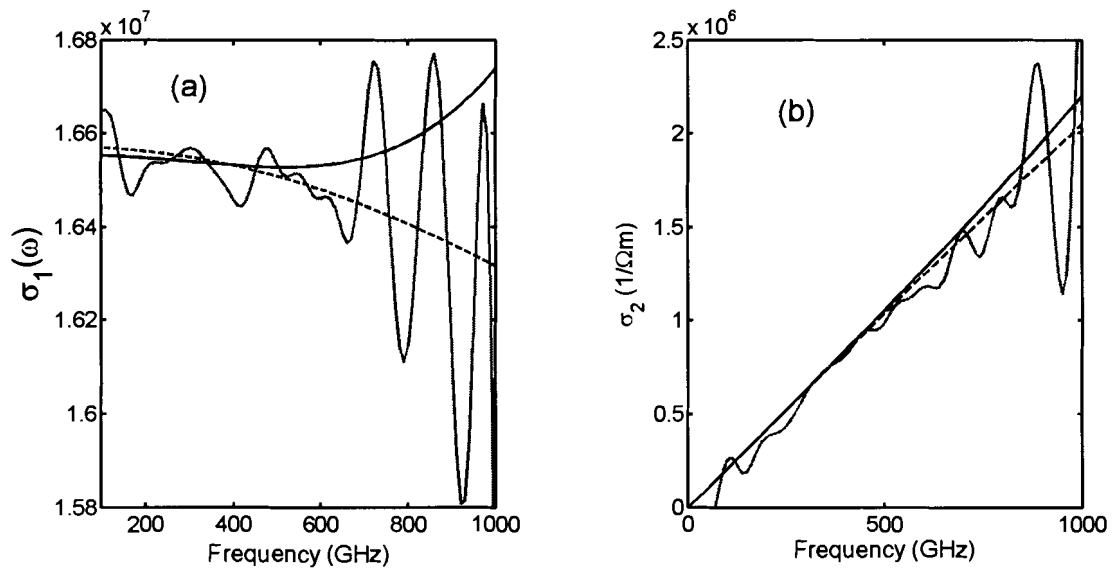

Figure A.2: Real (a) and imaginary (b) parts of the conductivity. The solid lines show the TSF and direct FFT methods while the dashed line indicates the theoretical curve.
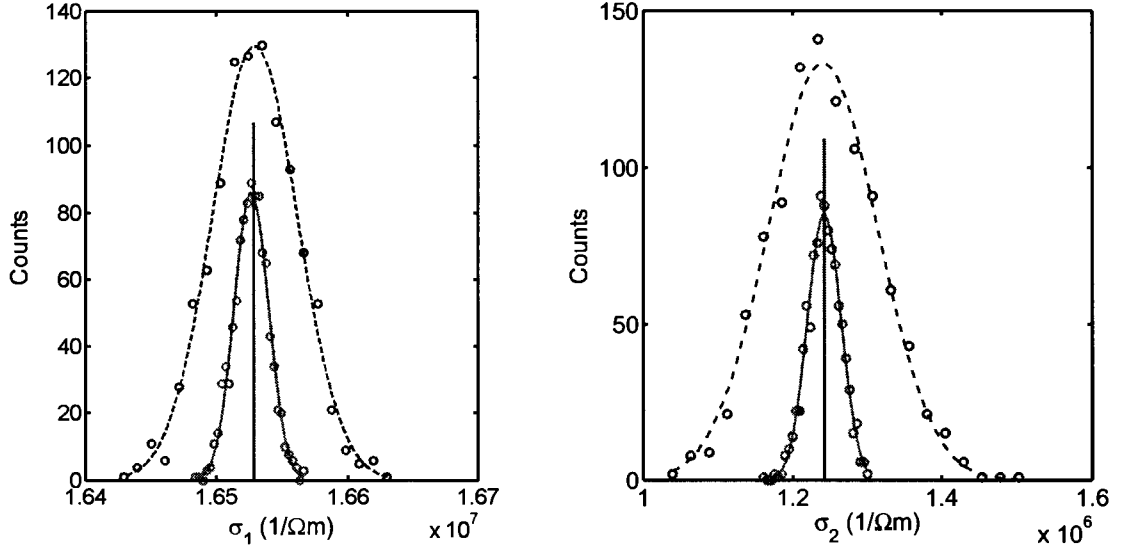
Figure A.3: Histograms for the real and imaginary parts of sigma. The solid and dashed lines show the gaussian fits to the FFT and TSF calculations. The exact values are given by the vertical solid lines.

The comparison made in Figure A.3 is not quite fair. The direct FFT calculation is not truncated in its order of frequency. Thus, a better comparison may be done by fitting the direct FFT calculation of the conductivity with the same form used for the TSF calculation. A choice must be made on the frequency range to fit over. We shall include three that seem appropriate; 100-700, 200-800, and 300-900 GHz. The center value shifts of σ_1 for both the FFT and TSF are less than 0.1% of the actual value of σ_1, while those for σ_2 are less than 5% of $\sigma_2(500\ GHz)$. Obviously, the shift in center value will not play much of a role. Figure A.4 shows the width as a function of frequency for the real (a) and imaginary (b) parts of the conductivity. The thick solid line indicates the TSF method while the thin solid, dashed, and dotted lines indicate the fittings over the FFT method from 100-700, 200-800, and 300-900 GHz, respectively. The TSF method now shows its advantage in dealing with the noise.

Figure A.5 shows the relative width of the Gaussian distributions as functions of frequency for τ and λ. Again, the thick solid line indicates the TSF method and the three other lines indicate the fits over the FFT method. For τ, the width of the distribution is
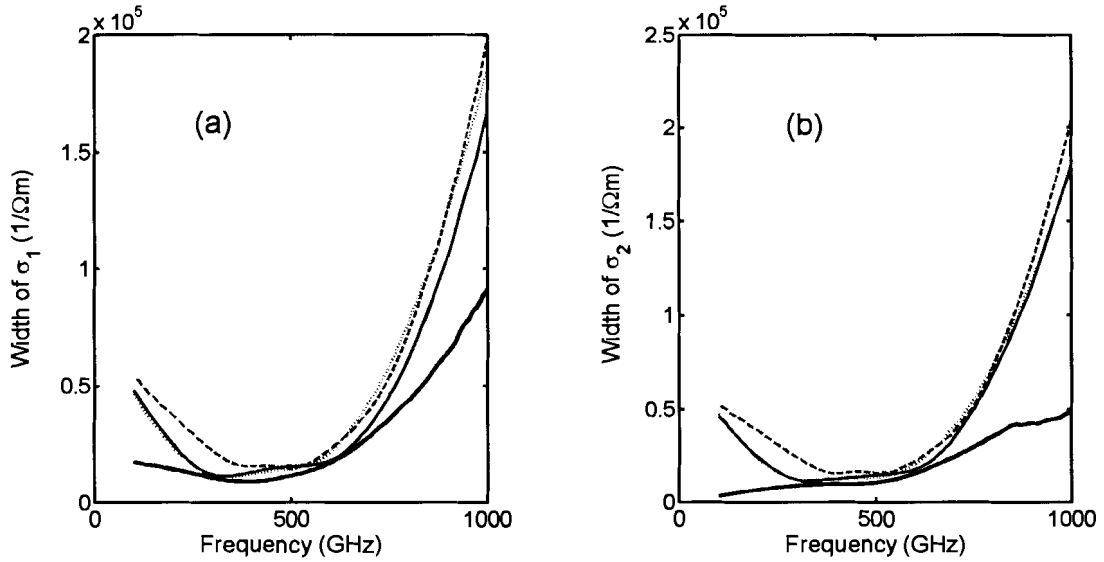
Figure A.4: Widths of the distributions for the real (a) and imaginary (b) parts of the conductivity as a function of frequency.

small for both methods. However, the width of the distribution for λ in the TSF method is substantially smaller, particularly in the low and high frequency regions.

The reduction in the width is equivalent to reducing the error bars associated with the time-frequency transformation. In this sense, the TSF method is promising. However, we have found it to be of little use for the data presented in this thesis. In particular, the scatter in the temperature dependence of λ is not improved. This is because there exists a noise contribution in the phase. The TSF method is only adept at eliminating the adverse effects of random noise in the time-frequency transformation. Further work must be done in order to fully understand the advantages of the TSF method and to explore other methods of analysis.
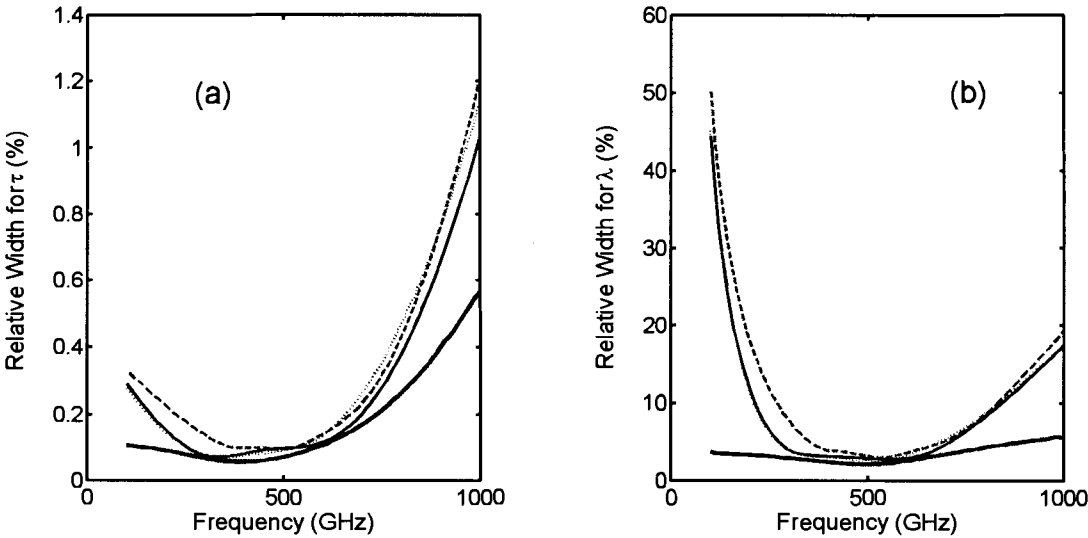
Figure A.5: Widths of the Gaussian distribution for τ (a) and λ (b) as a function of frequency for the TSF (thick solid) and fits of the FFT.

Appendix B

Insignificance of Magnetic Contributions

In order to extract the electrical conductivity from the terahertz transfer coefficient t_{thz} in Chapter 3, we made use of Equation 3.16. This relation is only valid when the magnetic permeability $\mu(\omega)$ can be approximated by the permeability of free space μ_0. Since chromium is magnetic, we must justify this approximation. The following outlines the general argument appropriate for chromium in our experimental frequency range of 0.1-1.0 THz.

In general, the magnetic and dielectric susceptibilities (χ_m and χ_d) for a metal have very different characteristic frequency scales. At frequencies above the microwave region, the magnetic susceptibility is small, with the largest contributions coming from magnetic resonances. In the case of chromium, these are antiferromagnetic resonance (AFMR) modes. Thus, we can estimate an upper bound on χ_m in chromium by assuming an AFMR occurs in our experimental frequency range. Including a damping rate γ, the zero-field magnetic susceptibility near the AFMR is given by

$$\chi_m = -\frac{2\gamma_L^2 K}{\omega^2 - \omega_c^2 - i\omega\gamma}$$

(B.1)

where γ_L is the Larmor frequency, K is the anisotropy, and ω_c is the zero-field AFMR frequency [21]. The damping rate γ accounts for the finite lifetime of the $q = 0$ magnons. The resonance frequency can be written as $\omega_c = \gamma_L(2\lambda K)^{1/2}$, where λ is the mean field exchange parameter [21]. Thus, at resonance, the magnitude of the susceptibility is given by

$$|\chi_m| = \frac{\omega_c}{\lambda\gamma}$$

(B.2)

70

Assuming $\omega_c/\gamma \sim 10$, which is very large for magnons in a metal, we have $|\chi_m| \sim 1/\lambda$. The value of λ is on the order of 10^4, so our conservative estimate is $|\chi_m| \sim 10^{-4}$. This contribution would modify the conductivity calculated using Equation 3.16 by only 0.01%, which is negligible in our experiment.

Bibliography

[1] NBS Technical Code 365, *Survey of electrical resistivity measurements*, Feb. 1968.

[2] Jr. A. S. Barker and J. A. Ditzenberger, Physical Review B **1** (1970), 4378.

[3] J. W. Allen and J. C. Mikkelsen, Physical Review B **15** (1977), 2952.

[4] P. B. Allen, Physical Review B **3** (1971), 305.

[5] ————, cond-mat/0407777 (2004).

[6] Sigurds Arajs, Canadian Journal of Physics **47** (1969), 1005.

[7] N. W. Ashcroft and N. D. Mermin, *Solid state physics*, Holt, Rinehart and Winston, 1976.

[8] D. H. Auston, IEEE Journal of Quantum Electronics **QE-19(4)** (1983), 649.

[9] O. Rapp B. Sundqvist, J. Neve, Physical Review B **32** (1985), 2200.

[10] K. P. Cheung D. H. Auston and P. R. Smith, Applied Physics Letters **49(3)** (1984), 286.

[11] O. V. Dolgov and S. V. Shulga, Journal of Superconductivity **8** (1995), 611.

[12] A. V. Silhanek et al, Cond-mat/0407737 (2004).

[13] A. Yu. Gerasimenko et al, Physics of the Solid State **44** (2002), 1208.

[14] J. C. Diels et al, Applied Optics **24(9)** (1985), 1270.

[15] M. A. Ordal et al, Applied Optics **24** (1985), 4493.

[16] N. Bouad et al, Journal of solid State Chemistry **173** (2003), 189.

[17] R. H. Willens et al, Physical Review B **25** (1982), 290.

[18] S. D. Brorson et al, Physical Review Letters **64** (1990), 2172.

[19] S. Venkataraj et al, Journal of Vacuum Science Technology A **19** (2001), 6.

[20] B. Farnworth and T. Timusk, Physical Review B **14** (1976), 5119.

[21] Simon Foner, *Magnetism*, vol. 1, Academic Press, 1963.

[22] G. Grimvall, *The electron-phonon interaction in metals*, North-Holland Publishing Company, 1981.

[23] E. G. Maksimov H. K. Kaufmann and E. K. H. Salje, Journal of Superconductivity **11** (1998), 755.

[24] J. T. Chen J. D. Leslie and T. T. Chen, Canadian Journal of Physics **48** (1970), 2783.

[25] Zdenek Knittl, *Optics of thin films*, John Wiley and Sons, 1976.

[26] W.L. McMillan and J.M. Rowell, Phys. Rev. Lett. **14** (1965), 108.

[27] Hazime Mori, Progress of Theoretical Physics **34** (1965), 399.

[28] Matin C. Nuss and Joseph Orenstein, *Topics in applied physics*, vol. 74, Springer-Verlag, 1998.

[29] A. W. Overhauser, Physical Review **128** (1962), 1437.

[30] H. M. Pickett S. Matsuura P. Chen, J. C. Pearson and G. A. Blake, Astrophys. J. Suppl. **128** (2000), 371.

[31] Edward D. Palik, *Handbook of optical constants*, Academic Press, Inc., 1985.

[32] D. Pines and P. Nozières, *The theory of quantum liquids*, W. A. Benjamin, Inc., 1966.

[33] R. E. Prange and L. P. Kadanoff, Physical Review **134** (1964), 566.

[34] A.V. Puchkov, D.N. Basov, and T. Timusk, J. Phys.: Cond. Matt. **8** (1996), 10049–10082.

[35] O. E. Martinez R. L. Fork. and J. P. Gordon, Opt. Lett. **9(5)** (1984), 150.

[36] H. Sher, Physical Review Letters **25** (1970), 759.

[37] S.V. Shulga, O.V. Dolgov, and E.G. Maksimov, Physica C **178** (1991), 266–274.

[38] A. Smakula, Physical Review **99** (1955), 1737.

[39] B. E. Warren, *X-ray diffraction*, Addison-Wesley Publishing Company, 1969.

[40] J. M. Ziman, *Principles of the theory of solids*, Cambridge, 1972.